

A Statistical Study of the Moon's Magnetotail Plasma Environment

Lucas Liuzzo¹, Andrew R. Poppe¹, and Jasper S. Halekas²

¹Space Sciences Laboratory, University of California, Berkeley, California

²Department of Physics and Astronomy, University of Iowa, Iowa City, Iowa

Key Points:

- We use ten years of data from the THEMIS-ARTEMIS mission to constrain the lunar plasma environment within the terrestrial magnetotail
- We identify three predominant distributions of the magnetotail plasma, corresponding to the magnetosheath, lobes, and plasma sheet
- For these conditions, we calculate statistical properties of the local magnetic field, plasma bulk velocity, number density, and temperature

13 **Abstract**

14 This study investigates the lunar plasma environment when embedded within Earth's
 15 magnetotail. We use data from ten years of tail crossings by the Acceleration, Recon-
 16 nection, Turbulence, and Electrodynamics of the Moon's Interaction with the Sun (ARTEMIS)
 17 spacecraft in orbit around the Moon. We separate the plasma environments by magnetosheath-
 18 like, magnetotail lobe-like, and plasma sheet-like conditions. Our findings highlight that
 19 the lobe-like plasma is associated with low densities and a strong magnetic field, while
 20 the plasma sheet is characterized by higher densities and a weaker magnetic field. These
 21 regions are flanked by the fast, predominantly tailward flows of the terrestrial magne-
 22 tosheath. During a single lunar crossing, however, the magnetotail displays a wide range
 23 of variability, with transient features—including reconnection events—intermixed between
 24 periods of lobe-like or sheet-like conditions. We compare and contrast the Moon's local
 25 magnetotail plasma to the environments near various outer-planet moons. In doing so,
 26 we find that properties of the ambient lunar plasma are, at times, unique to the terres-
 27 trial magnetotail, while at others, may resemble those near the Jovian, Saturnian, and
 28 Neptunian moons. These findings highlight the complementary role of the ARTEMIS
 29 mission in providing a deeper understanding into the plasma interactions of the outer-
 30 planet moons.

31 **1 Introduction**

32 During its 29-day orbit, the Moon is exposed to a wide range of plasma environ-
 33 ments. While located outside of Earth's magnetosphere, the high density, super-Alfvénic
 34 flows of the solar wind continually bombard the Moon. The resulting interaction has been
 35 well-studied: an extended wake forms downstream of the Moon (e.g., Michel, 1968; Ness,
 36 1965), characterized by a drop in the solar wind number density and associated with an
 37 enhanced magnetic field (Ness, 1972; Bosqued et al., 1996; Holmström et al., 2012; Zhang
 38 et al., 2014; Halekas et al., 2015). When located within Earth's magnetosphere, however,
 39 the lunar plasma environment is vastly different; after transiting through the shocked
 40 magnetosheath plasma, the magnetotail can be characterized by nominally lobe-like and
 41 sheet-like plasma (Hardy et al., 1976; Sibeck & Murphy, 2021). Previous studies have
 42 applied data from multiple spacecraft missions to study the properties of these plasma
 43 populations using a handful of tail crossings. Behannon (1970) used data from the Ex-
 44 plorer 33 and Explorer 35 missions to characterize the magnetic field within the tail plasma

sheet, and found that it is associated with a broad region of reduced magnetic field magnitude that is (on average) oriented northward out to a distance of $70R_E$ (radius of Earth $R_E = 6,378$ km) downstream of the planet. Further studies by, e.g., Slavin et al. (1985) and Vasko et al. (2015) have investigated the structure of the tail plasma out to even greater distances of up to $130R_E$, using data from the International Sun-Earth Explorer-3 (ISEE-3) and Geotail missions, respectively. Additional studies of the magnetotail lobes have shown that the plasma typically flows downtail (Hardy et al., 1976) along well-ordered magnetotail lobe field lines mainly oriented sunward/anti-sunward (Meng & Anderson, 1974; Yamamoto et al., 1994); additional components to the magnetotail field are strongly correlated with the direction of the interplanetary magnetic field (e.g., Hardy et al., 1979; Cowley, 1981a, 1981b; Sibeck et al., 1985).

Using these missions to obtain the long-term properties of the lunar magnetotail plasma environment during tail crossings is challenging: the data are restricted by the orbital properties of the spacecraft (e.g., ISEE-3 and Geotail were at times located more than $200R_E$ from Earth) or limited to the brief observational windows when the Moon was located within the magnetotail during the mission's lifetime (e.g., only a few hundred hours of data were collected within the lobes by the instruments placed on the lunar surface during the Apollo missions; see, e.g., Hardy et al., 1976). Therefore, although the Moon spends approximately a quarter of each lunation within the terrestrial magnetotail, the statistical properties of the magnetotail plasma along the lunar orbit are only weakly constrained.

Unlike these missions which spent brief periods of time near the Moon's position, the Acceleration, Reconnection, Turbulence, and Electrodynamics of the Moon's Interaction with the Sun (ARTEMIS) mission was placed into lunar orbit (Angelopoulos, 2011). Originally part of the Time History of Events and Macroscale Interactions during Substorms (THEMIS) mission, the two ARTEMIS probes (P1 and P2) have spent more than ten years exposed to the lunar plasma environment since their orbital insertion in 2011. The goal of this study is therefore to understand the long-term average properties of the Moon's plasma environment while transiting the terrestrial magnetotail using the vast data set obtained during the entire (to date) ARTEMIS mission while the probes were located within Earth's geomagnetic tail. In section 2, we present data obtained by the probes during a typical tail crossing in order to identify characteristic signatures of the magnetotail plasma. We then present data from 126 tail crossings during the past ten

78 years of the mission in section 3, where we investigate properties of the magnetic field,
 79 bulk velocity, and density of the local magnetotail plasma, and perform a statistical anal-
 80 ysis of the environment to which the Moon is exposed during these crossings. Finally,
 81 section 4 concludes our study and places the lunar plasma environment within the ter-
 82 restrial magnetotail into a broader context by comparing and contrasting it with the plasma
 83 environments near various outer-planet moons.

84 2 Case Study of a Magnetotail Crossing

85 The ARTEMIS probes orbit the Moon along elliptical trajectories with periods of
 86 approximately 24–26 h (Angelopoulos, 2011). Each probe has a perilune that varies in
 87 altitude from approximately 10 km to 1,000 km, with an apolune on the order of 19,000
 88 km. For this study, we present data from the Flux Gate Magnetometer (FGM; Auster
 89 et al., 2008), the Electric Field Instrument (EFI; Bonnell et al., 2008), and the Electro-
 90 static Analyser (ESA; McFadden, Carlson, Larson, Ludlam, et al., 2008) collected by the
 91 identically instrumented probes.

92 Before using the ten-year-long ARTEMIS data set to study the properties of the
 93 lunar magnetotail environment, we first highlight the key aspects of the various plasma
 94 environments to which the Moon is exposed during a typical crossing of the terrestrial
 95 magnetotail. For approximately one quarter of each lunation, the Moon (and the two
 96 ARTEMIS probes) travels through the Earth’s magnetotail at approximately $60R_E$ down-
 97 stream of the planet. Figure 1 displays ARTEMIS P1 observations from midnight on Oc-
 98 tober 24, 2012 to midnight on November 03, 2012, during such a passage. The magne-
 99 tosphere during this period was relatively calm, with estimated Planetary K and A in-
 100 dices between $0 \leq K_p \leq 4$ and $2 \leq A_p \leq 17$. Shown from top to bottom in Figure 1
 101 are measurements of the magnetic field \mathbf{B} , the ion and electron differential energy fluxes,
 102 the plasma number density n calculated using the reduced electron density product from
 103 the ESA, the ion bulk velocity \mathbf{V} , the ion and electron temperatures, the plasma beta,
 104 and the Alfvénic Mach number M_A as observed by ARTEMIS. Here, the Alfvénic Mach
 105 number is the ratio between the magnitudes of the bulk plasma flow velocity and the Alfvén
 106 velocity (given by $\mathbf{V}_A = \mathbf{B}/\sqrt{n\mu_0}$ with mass m), while the plasma beta is given by
 107 $\beta = 2\mu_0 n k_B T / |\mathbf{B}|^2$. Note that for this study, we assume that all ions detected within
 108 the magnetotail are protons with mass $m = 1$ amu. For times where the ESA detects
 109 only background ion counts, the total plasma beta displayed in Figure 1 is assumed to

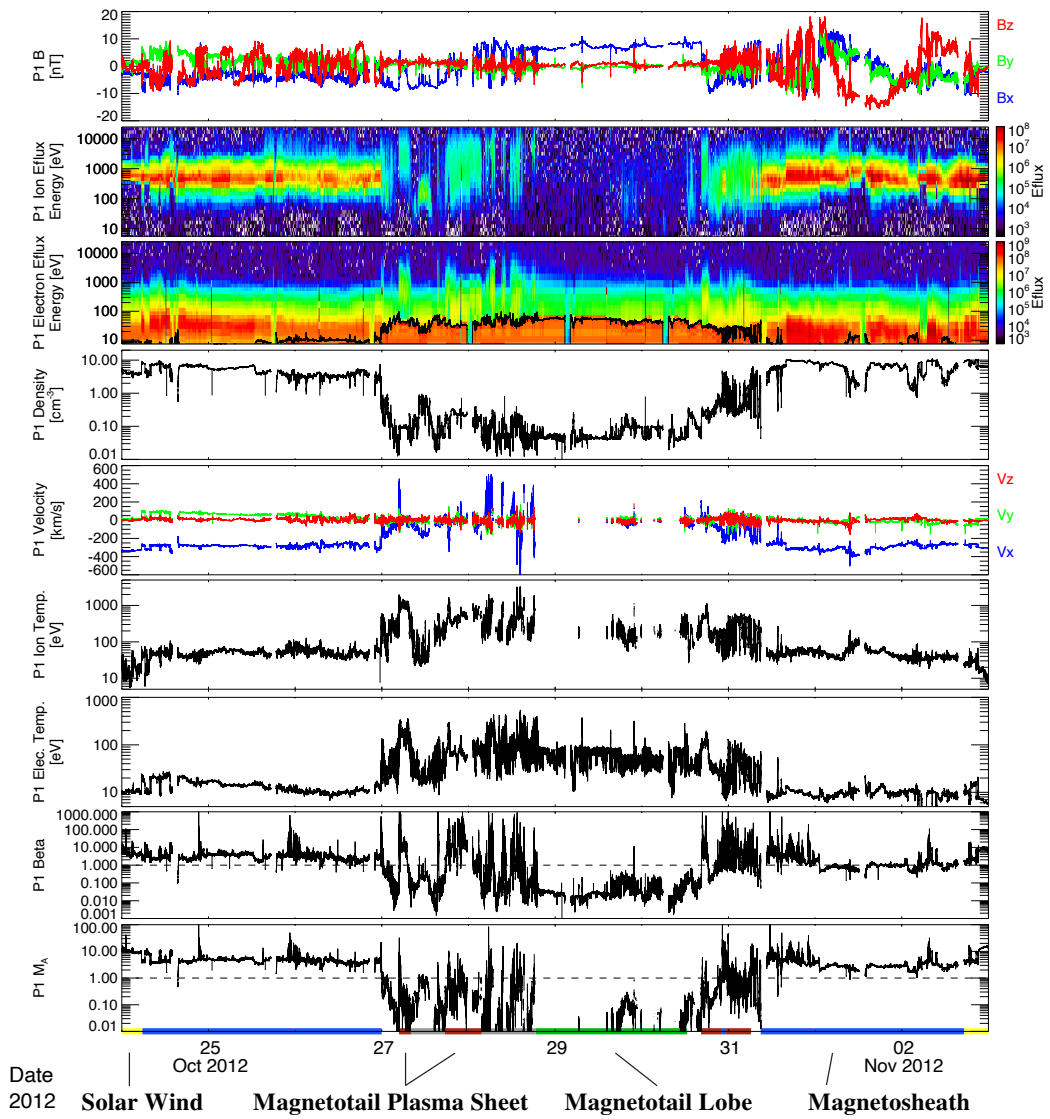


Figure 1. ARTEMIS P1 observations during a typical passage through Earth's magnetotail between 24 October 2012 and 03 November 2012 (see text for further detail). Colored bars at the bottom illustrate times when the probe was exposed to the (yellow) solar wind plasma, (blue) terrestrial magnetosheath, (red) magnetotail plasma sheet, and (green) magnetotail lobes. Gray bars denote other, more dynamic events (see text).

equal the electron plasma beta. The solid black line over-plotted onto the electron spectra denotes the spacecraft potential; fluxes below this line are dominated by spacecraft photoelectrons and are thus not geophysical (see McFadden, Carlson, Larson, Bonnell, et al., 2008).

In Figure 1 and for the remainder of the paper, components of vector quantities are given in the Geocentric Solar Ecliptic (GSE) coordinate system. In this system, the unit vector $+\hat{\mathbf{z}}$ is parallel with the (upward) normal to Earth's ecliptic plane, $+\hat{\mathbf{x}}$ points Sunward, and $+\hat{\mathbf{y}}$ completes the right-handed set. Note that to ensure accurate calculations of the plasma moments, times when the ARTEMIS ion ESA detected only background counts have been removed from Figure 1, which we define as an integrated ion energy flux below $1.5 \cdot 10^5 \text{ eV cm}^{-2} \text{ s}^{-1} \text{ sr}^{-1}$ (corresponding to a number density on the order of $n \approx 0.01 \text{ cm}^{-3}$). In addition, we have removed measurements obtained when the P1 probe was located within the Moon's shadow from the data set, which affects the accuracy of the magnetic field vector and the particle moments (see Georgescu et al., 2011), as well as measurements within $0.5R_M$ of the Moon's surface ($R_M = 1,737 \text{ km}$) in order to exclude any lunar perturbations on the local plasma environment (e.g., Poppe et al., 2012; Halekas et al., 2013).

Besides the solar wind plasma at the edges of the ten-day time period (see yellow bars at the bottom of Figure 1), three distinct, clearly identifiable plasma environments are visible in the ARTEMIS data set. The first environment of note is the terrestrial magnetosheath, detected just after midnight on October 24, 2012 while the P1 probe was exposed to the dusk flank of Earth's magnetosheath. As seen in Figure 1, the ion and electron temperatures of this shocked plasma reached values of $T_i \approx 40 \text{ eV}$ and $T_e \approx 20 \text{ eV}$ (i.e., warmer than in the solar wind), with a density of $n \approx 4\text{--}8 \text{ cm}^{-3}$ and an anti-Earthward bulk velocity of $\mathbf{V} \approx -250\hat{\mathbf{x}} \text{ km/s}$. The Alfvénic Mach number and plasma beta each exceed a value of 1 within the sheath. ARTEMIS again crossed the terrestrial magnetosheath on the dawn flank just before 12:00 on October 31, during the probe's exit of the magnetotail on the terrestrial dawn side. The blue bars at the bottom of Figure 1 highlight the locations where this sheath plasma was observed during the crossing.

The second region encountered by the probe during this period is the magnetotail plasma sheet, as observed post-midnight on October 27 after crossing the magnetopause.

This environment is hotter than the magnetosheath plasma (reaching temperatures of $T_i \gtrsim 1000$ eV and $T_e \gtrsim 100$ eV) but with comparatively reduced velocities, which remained below approximately $|\mathbf{V}| < 100$ km/s. Concurrently, the magnetic field was typically lower in magnitude than in the sheath ($|\mathbf{B}| < 5$ nT) with all three components close to zero. During the magnetotail crossing, ARTEMIS observed this plasma population multiple times, near 12:00 UT and 18:00 UT on October 27 and from 18:00 UT on October 30 to 08:00 UT on October 31 (see the red bars in Figure 1).

The third notable region detected by the P1 probe during this tail crossing is associated with the Moon's location within the northern lobe of Earth's magnetotail. This extended, quiescent period during which the probe detected the terrestrial magnetotail lobe plasma occurred from approximately 19:00 UT on October 28 to 12:00 UT on October 30 (see the green bar at the bottom of Figure 1). The most striking feature during this time period was the low number density ($n < 0.1$ cm $^{-3}$) associated with only minimal particle fluxes (see the second row of Figure 1). Note that the low (and at times, non-existent) ion fluxes within the magnetotail lobes observed by ARTEMIS make determination of the plasma moments difficult, and sometimes impossible, in the lobes (see also, e.g., Cao, Halekas, Chu, et al., 2020; Liuzzo, Poppe, et al., 2021). The magnetic field during this period was directed almost entirely Earthward, with $B_x > 0$ and a magnitude of $|\mathbf{B}| \approx 10$ nT, and the values of β and M_A were well below 1 within this region.

In addition to the magnetosheath, magnetotail plasma sheet, and tail lobe environments, the ARTEMIS data in Figure 1 also show evidence of short and often more dynamic features during the crossing (see the gray bars along the bottom of the figure). For example, near 12:00 UT on October 27, P1 observed an ion population with $n \approx 0.5$ cm $^{-3}$ and a tailward velocity of $V_x \approx -150$ km/s, in the presence of generally lobe-like magnetic fields with $B_x < 0$ (indicating the southern tail lobe). This population likely corresponds to the low-latitude boundary layer or, alternatively, the low-latitude plasma mantle (Wang et al., 2014), whereby magnetosheath plasma has entered the magnetotail proper across the magnetopause and continues to convect downstream. Another, more dynamic period of note occurs between 06:00 and 18:00 UT on October 28. Here, ARTEMIS observed a series of high velocity plasma flows ($|\mathbf{V}|$ up to 600 km/s) alternately directed Earthward then tailward, with high temperatures ($T_e \gtrsim 300$ eV and $T_i \gtrsim 1000$ eV) and low densities ($n \lesssim 0.2$ cm $^{-3}$). These high velocity flows are likely ejecta

175 originating from reconnection exhausts in the middle-magnetotail region (e.g., Artemyev,
 176 Angelopoulos, Runov, & Vasko, 2017; Runov et al., 2018; Kiehas et al., 2018; Wang et
 177 al., 2020). The frequent reversal of flow from Earthward to tailward directions (and vice
 178 versa) possibly indicates the repeated movement of the reconnection X-line past the ARTEMIS
 179 probes (e.g., Wang et al., 2020) located approximately $60R_E$ downtail.

180 Figure 1 highlights the various plasma populations to which the Moon is exposed
 181 during a typical crossing of the terrestrial magnetotail: flanked by fast flows of the mag-
 182 netosheath, lobe-like and sheet-like conditions dominate large portions of the plasma en-
 183 vironment, with dynamic variability on shorter time scales. However, the rich ARTEMIS
 184 data set allows us to perform a statistical analysis of all lunar crossings of the tail over
 185 the past ten years to better characterize the long-term averages of these distinct plasma
 186 populations to which the Moon is exposed during nearly a quarter lunation.

187 3 The Moon in Earth's Magnetotail

188 We use 126 magnetotail crossings from over ten years of ARTEMIS observations
 189 for this analysis—beginning with the crossing on August 08, 2011 and ending with the
 190 crossing on November 14, 2021. For each probe, we define the start of the magnetotail
 191 crossing as the probe's final passage through Earth's bow shock on the terrestrial dusk
 192 side of the planet, and the end as the first encounter with the bow shock on the dawn
 193 side. Although this filters out some observations due to, e.g., multiple bow shock cross-
 194 ings during entry into the tail, this ensures that the data set contains only magnetotail
 195 plasma. To ensure uniform sampling rates between the P1 and P2 probes, the measure-
 196 ments from each crossing are interpolated to a 4-second cadence. As a whole, this data
 197 set comprises more than 50,000 h of ARTEMIS data that are available to constrain the
 198 near-lunar plasma environment within the magnetotail.

199 In order to separate the different types of plasma regimes to which the Moon is ex-
 200 posed during a terrestrial magnetotail crossing (see, e.g., Figure 1), we establish a set
 201 of requirements that categorize the ARTEMIS observations within the magnetotail as
 202 either “lobe-like,” “sheet-like,” or “sheath-like.” To categorize the magnetotail plasma
 203 into lobe-like and sheet-like conditions, we require that the probe was located within 20°
 204 in longitude of the local midnight meridian (i.e., the GSE $-x$ axis) at the time of the
 205 measurement. This requirement avoids any bias in sampling between the terrestrial dawn

and dusk hemispheres of the magnetotail and prevents magnetosheath plasma from being incorrectly classified as lobe-like or sheet-like. This latter point is consistent with studies by Mieth et al. (2019) and Nguyen et al. (2021) who have shown that ARTEMIS rarely crosses the magnetopause within 20° of the Sun-Earth line near the lunar distance of $\sim 60R_E$ downstream of Earth. Note, however, that this filter does not correct for the magnetotail aberration (e.g., Gencturk Akay et al., 2019), which makes it difficult to completely exclude all of the plasma that is neither lobe-like nor sheet-like from the data set. Using the crossing shown in Figure 1 as an example, P1 was within $\pm 20^\circ$ of the Sun-Earth line from approximately 22:15 on October 27, 2012 through 13:30 on October 31, 2012. Hence, out of nearly 240 h of data during this crossing, a few hours of magnetosheath plasma is still present even after this filter is applied.

The terrestrial magnetotail lobes are characterized by a magnetic field that mainly points either toward or away from Earth (i.e., the lobe field is predominantly aligned along $\pm\hat{\mathbf{x}}$). Hence, to identify lobe-like conditions, we define \mathbf{b}_t to be the moving average of the magnetic field centered over four time windows: $t = 30$ minutes, $t = 60$ minutes, $t = 90$ minutes, and $t = 120$ minutes. To ensure that the field is predominantly aligned along $\pm\hat{\mathbf{x}}$ (i.e., is consistent with the lobes), we require B_x to be the dominant component during each of these windows; i.e., $|b_{x,t}| > \psi_t |\mathbf{b}_t|$ for a threshold value of ψ_t . For the moving average over the smallest window, we set the empirically determined threshold parameter to its highest value of $\psi_{30} = 0.93$; i.e., within ± 15 minutes of the measurement, 93% of the field must have been along the $\pm\hat{\mathbf{x}}$ direction. This allows for the algorithm to capture rapid transitions from non-lobe-like regions (e.g., within the magnetosheath) into the lobe. However, for the next three windows, the threshold values are slightly reduced to $\psi_{60} = 0.92$, $\psi_{90} = 0.91$, and finally $\psi_{120} = 0.90$. This ensures that the field is sustained along the Earthward/anti-Earthward direction for an extended time and excludes periods where the magnetotail field may happen to be only briefly x -aligned, while still allowing for more gradual transitions into non-lobe-like regions of the magnetotail. In addition to the above, we also require that the value of $|\mathbf{B}|$ at any given point in time is within $\pm 5\%$ of $|\mathbf{b}_t|$ for each of the four time windows. Hence, this approach prevents potentially misidentifying rapid fluctuations in the field as the magnetotail lobes, during time periods that may otherwise be lobe-like (e.g., during the reconnection events detected by ARTEMIS from 06:00-18:00 on October 28; see Figure 1).

238 Observations within the magnetotail plasma sheet are characterized by a reduc-
239 tion in the magnetic field magnitude (see, e.g., red bars in Figure 1). Hence, to identify
240 sheet-like conditions, we perform a separate filtering of the ARTEMIS data, requiring
241 $|\mathbf{b}_{30}| < 0.75|\mathbf{b}_{120}|$. This filter ensures a rapid and sustained drop in the moving aver-
242 age of $|\mathbf{B}|$, such that the 30-minute average of magnetic field magnitude is at least 75%
243 lower than the 120-minute average. Note that this filter therefore excludes encounters
244 with the plasma sheet that may last multiple hours; however, there are still a sufficient
245 number of plasma sheet-like events over the ten-year ARTEMIS mission to obtain re-
246 liable statistics for this magnetotail region. Note that while the method defined above
247 is likely not a unique solution to identify lobe- and sheet-like fields, the overall effect of
248 using a different set of persistence filters (e.g., by changing the window sizes used for the
249 moving averages or by setting different threshold values) is only minor on the ten-year-
250 long data set.

251 Conversely, to reliably identify magnetosheath-like conditions of the magnetotail
252 plasma, we require ARTEMIS to be separated by *at least* 20° longitude from either side
253 of the local midnight meridian, thereby excluding the majority of lobe-like and sheet-
254 like regions. The only additional requirement to be classified as sheath-like is that the
255 plasma number density satisfies $n \geq 1 \text{ cm}^{-3}$, effectively including all boundary layers
256 in the sheath-like classification. Importantly, a given observation may only be classified
257 as either lobe-, sheet-, or sheath-like, but not any combination thereof. Finally, we note
258 that the colored bars presented along the bottom of Figure 1 are not identified using the
259 automated filtering described above.

260 The distribution of the ARTEMIS observations within the magnetotail as a func-
261 tion of phase angle, and the resulting classifications for the three regions considered in
262 this study, are displayed in Figure 2. Phase increases in a counter-clockwise direction
263 against the Sun-Earth line (i.e., the $+x$ axis of the Geocentric Solar Ecliptic system) as
264 viewed from above the ecliptic plane, such that the terrestrial dusk terminator (the $+y$
265 axis of GSE) coincides with an angle of 90° , local midnight is located at 180° , and the
266 dawn terminator coincides with 270° . As shown by the black outlines in Figure 2, the
267 distribution of measurements is nearly uniform across all phase angles within the mag-
268 netotail (at just under 2 million measurements per bin). However, the aberrated tail struc-
269 ture is apparent, with a shift in the distribution toward dusk (i.e., toward phase angles
270 below 180°), especially visible for magnetosheath-like conditions (filled blue bars in the

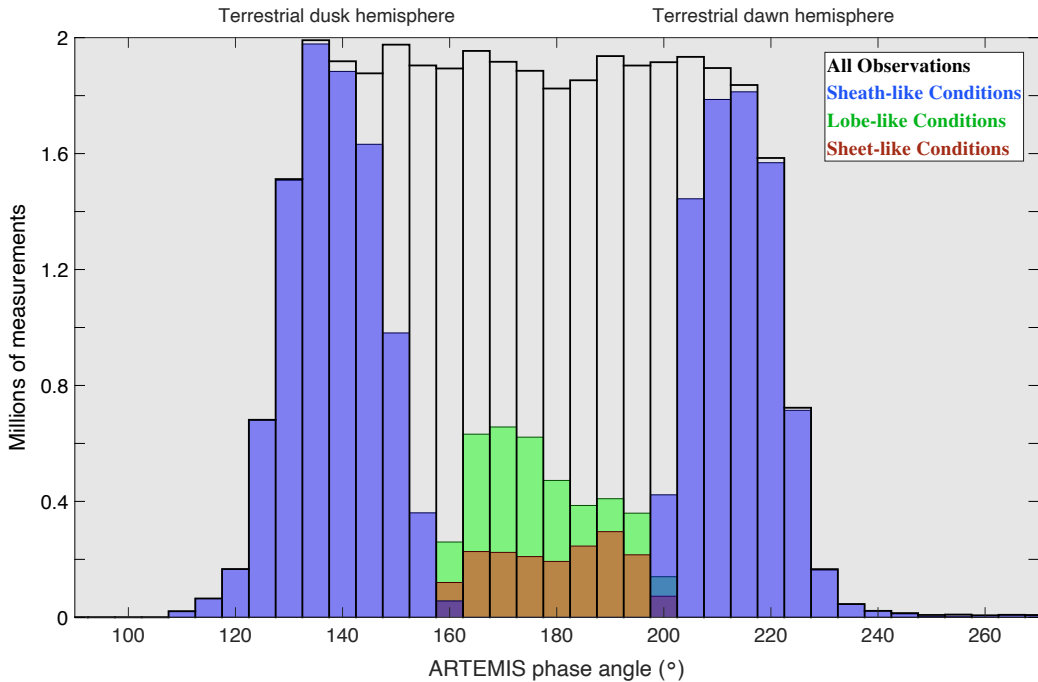


Figure 2. Overlapping histograms of the ARTEMIS observations within the magnetotail as a function of lunar phase angle separated into 2° bins. Colors correspond to the three magnetotail regions considered in this study: (blue, filled) magnetosheath-like conditions, (green, filled) magnetotail lobe-like conditions, and (red, filled) magnetotail plasma sheet-like conditions. The total number of observations within each bin is indicated by the black outlines.

figure). In addition, Figure 2 illustrates that nearly all observations with the probes separated by more than 20° in longitude from local midnight (i.e., phase angles below 160° and greater than 200°) are classified as magnetosheath-like conditions. Approximately one-quarter of all observations are classified as magnetotail lobe-like (with a slight bias toward dusk; see the filled green bars in the figure), while slightly over one-tenth of observations are classified as sheet-like (with no strong dusk/dawn asymmetry; filled red bars), thereby providing a sufficient number of measurements to accurately characterize these magnetotail regions. The remaining observations within 20° longitude of local midnight do not satisfy the set of filters given above, and are either less representative of the “pure” magnetotail lobes or plasma sheet (including, e.g., magnetosheath encounters within 20° of local midnight or fluctuations in the local environment due to transient plasma events), or are not readily classified as either of these regions (e.g., encoun-

ters with the low-latitude boundary layer or plasma mantle; see the regions denoted by
the gray bars along the bottom of Figure 1).

285 3.1 Properties of the magnetic field

286 Figure 3 displays heatmaps that illustrate the distribution of the magnetic field com-
287 ponents observed by ARTEMIS when located within Earth’s magnetotail. The top row
288 (panels a–c) includes data from the entire set of magnetotail crossings; i.e., from the fi-
289 nal bow shock encounter on the terrestrial dusk side to the first encounter on the dawn
290 side for all 126 events. The (a) left, (b) middle, and (c) right columns display the B_x -
291 B_y , B_x - B_z , and B_y - B_z magnetic field component distributions, respectively, accumulated
292 into linearly-spaced bins with a width and height of 0.2 nT. For each bin, the color scale
293 represents the percentage of time per bin that a given magnetic field component set (e.g.,
294 B_x - B_y in panel a) was observed out of the total number of measurements N . For data
295 from all of the crossings presented in the top row of Figure 4, $N = 45,306,095$. Con-
296 tours are included at order-of-magnitude spacing, with the outermost contour correspond-
297 ing to observations at the $10^{-3}\%$ threshold for each bin. As with the data shown in Fig-
298 ure 1, those times when the probes are located in the Moon’s shadow have been removed
299 from the respective data sets to ensure accuracy of the measurements (Georgescu et al.,
300 2011). In addition, we exclude data obtained within $0.5R_M$ of the surface to avoid con-
301 taminating the measurements with local perturbations originating from the lunar iono-
302 sphere (e.g., Zhou et al., 2013; Cao, Halekas, Poppe, et al., 2020).

303 To better understand the distinct plasma environments to which the Moon is ex-
304 posed during a tail crossing, Figure 3 also includes ARTEMIS observations from when
305 the probes were exposed to (d–f) magnetosheath-like, (g–i) magnetotail lobe-like or (j–
306 l) plasma sheet-like conditions only, after applying the filtering described in the previ-
307 ous section. Note that the total number of observations N is different for each of these
308 environments ($N = 18,001,866$ for sheath-like conditions, $N = 3,937,040$ for lobe-
309 like conditions, and $N = 1,803,624$ for sheet-like conditions).

310 Panels 3a and 3b show that B_x is broadly distributed within the magnetotail. The
311 largest fraction of observations is centered near $B_x \approx 0$ nT and extends beyond val-
312 ues of ± 10 nT; less frequently, this component reaches $|B_x| > 25$ nT. Panel 3a also high-
313 lights a slight asymmetry in B_y with respect to B_x , especially visible beyond $|B_x| \approx 10$

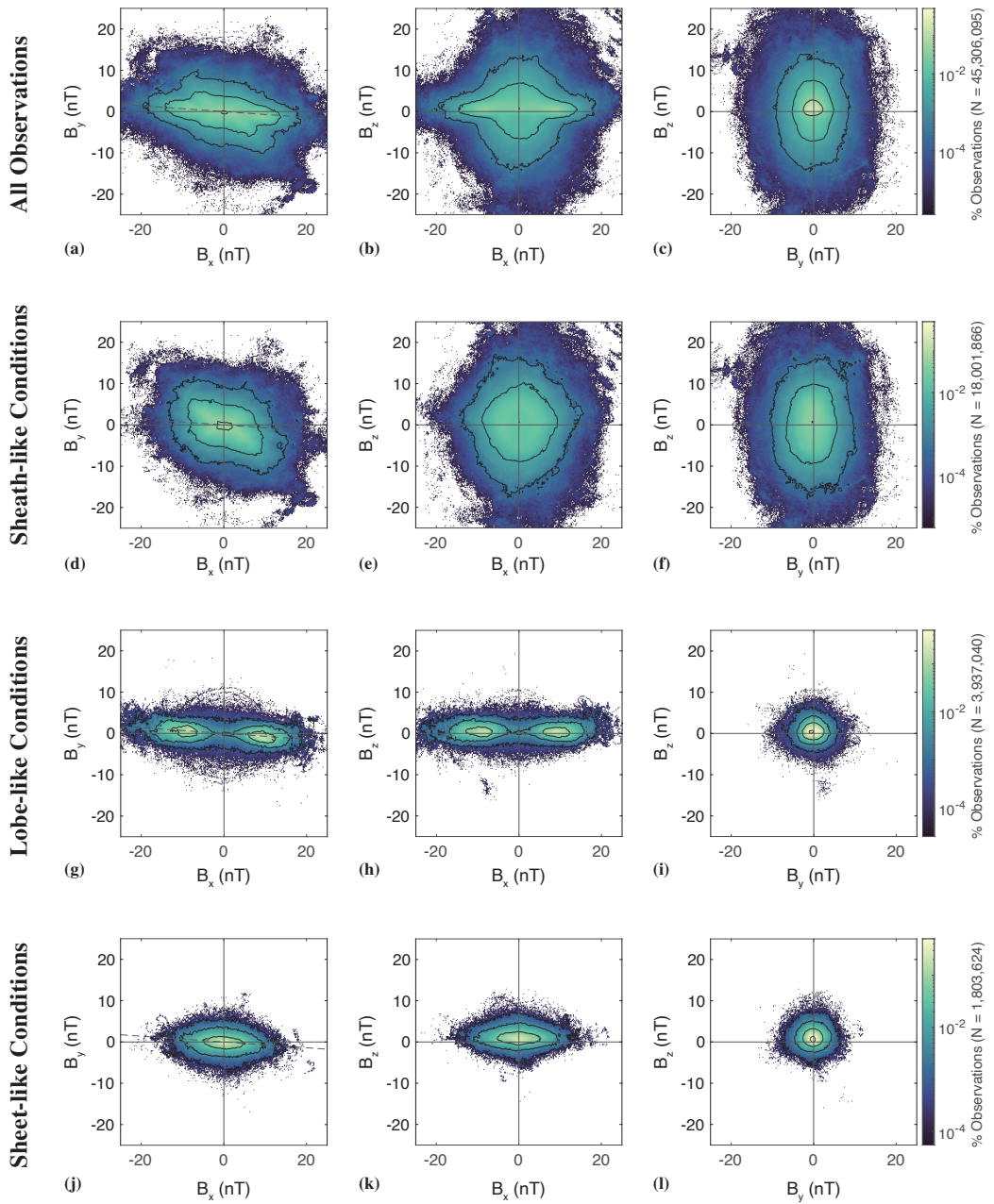


Figure 3. Distributions of the magnetic field components observed by ARTEMIS when located within Earth's magnetotail for (a–c) all conditions, (d–f) magnetosheath-like conditions only, (g–i) lobe-like conditions only, and (j–l) plasma sheet-like conditions only. Colors correspond to the percentage of total observations N per each bin, with N provided at the end of each row. Contours are drawn for each order of magnitude, with the outer-most contour corresponding to a value of $10^{-3}\%$ per bin. Note the differences in color scales and in the number of observations for each row.

nT. This effect is due to the aberration of the terrestrial magnetosphere (see also, e.g., Mihalov et al., 1968; Behannon, 1970; Kaymaz et al., 1994), whereby Earth's orbital velocity causes the down-tail magnetosphere to be tilted in the orbital plane against the Sun-Earth line by approximately 4° , although deviations beyond 20° have been observed resulting from non-radial components to the solar wind flow (Gencturk Akay et al., 2019). To guide the eye and more clearly illustrate this effect, panel 3a includes a dashed line that is tilted at an angle of 4° against the $B_y = 0$ line, which closely follows this asymmetry in the magnetic field components.

An additional feature of the magnetic field distribution within the magnetotail is a positive offset to the B_z component. Panels 3b and 3c show that B_z preferentially reaches values between $-1 \text{ nT} \leq B_z \leq 4 \text{ nT}$, centered around $B_z \approx +1 \text{ nT}$. In addition to these ten-year-long ARTEMIS observations, a similar signature of the positive B_z offset near the Moon has been observed (over shorter timescales) by the ISEE-3 spacecraft (e.g., Zwickl et al., 1984; Slavin et al., 1985), as well as by the Lunar Prospector and Kaguya missions (see Mittelholz et al., 2021). This positive bias in B_z is a signature of the orientation of Earth's magnetic dipole, which has a $B_z > 0$ component near the lunar orbit, and is visible for each of the three magnetotail conditions in this study (see Figure 3).

Panels 3b and 3c show that while B_z remains mostly within $\pm 10 \text{ nT}$, this component at times extends beyond $\pm 20 \text{ nT}$. This is most clearly visible at times when B_x and B_y are minimized, where the north/south component reaches values beyond $|B_z| > 20 \text{ nT}$. These tails—approaching large values in the B_z distribution—are indicative of the behavior of the magnetic field within the magnetosheath. The draping of the interplanetary magnetic field preferentially imparts a z -component to the magnetic field orientation (e.g., Behannon, 1968; Sibeck et al., 1986). This becomes especially clear in panels 3e and 3f, which shows the magnetic field for magnetosheath-like conditions alone. In panel 3d, the two inner-most contours—representing the most frequently observed set of magnetic field conditions—are more strongly tilted than the dashed line corresponding to a tail aberration angle of 4° . Rather, B_y is tilted by an angle of nearly 45° against the B_x component, consistent with the angle of the Parker spiral near Earth's orbit.

The number of ARTEMIS measurements within the magnetotail lobes shown in panels 3g–3i is reduced by more than a factor of 10 compared to the total number of points

obtained during the full data set. Here, the distributions illustrate that the magnetic field
 346 is mainly aligned with $\pm\hat{x}$ (as is expected given our filter identifying lobe-like conditions),
 347 reaching a value of $B_x \approx \pm 10$ nT for a large fraction of the time spent within the lobes.
 348 This field strength is approximately 33% lower than the magnitude of the B_x compo-
 349 nent observed during the early stages of the ISEE-3 mission: using four months of data
 350 from the spacecraft's initial magnetotail tail passes, Slavin et al. (1985) found that the
 351 magnitude of the terrestrial lobe field follows a power law decrease with increasing dis-
 352 tance downstream of Earth, reaching $|\mathbf{B}| \approx 15$ nT near $-60R_E$. Although the ISEE-
 353 3 measurements were obtained during solar maximum (just after its peak), the strength
 354 of the lobe field observed by ARTEMIS does not display a strong dependence on the most
 355 recent solar cycle. As with the full set of observations, the aberration of the magneto-
 356 tail is clearly visible in panel 3g, where B_y in the lobes is tilted by approximately 4° (see
 357 dashed line in the panel). The spread of B_y and B_z is now much narrower within the
 358 lobes, distributed nearly isotropically around 0 nT (see panel 3i). Here, the peak in lobe-
 359 like observations occur with $B_y = -1$ nT and $B_z = +1$ nT, with a limited number of
 360 measurements occurring while B_y or B_z exceeds ± 5 nT. Over the entire ten-year period,
 361 more than 99.999% of all observations with lobe-like fields satisfy -10 nT $\leq B_y, B_z \leq$
 362 10 nT.
 363

For the sheet-like conditions displayed in panels 3j–3l, the strength of the field drops
 364 by a factor of nearly 3, from an average value of $|\mathbf{B}| \approx 10$ nT in the lobes to a value
 365 of $|\mathbf{B}| < 4$ nT in the sheet. This is mainly driven by the lack of a strong x -aligned field
 366 component near the center of the plasma sheet, although each component of the mag-
 367 netic field is more focused near a value of ~ 0 nT. Few ARTEMIS observations of $|B_y|$
 368 or $|B_z|$ in the sheet exceed a value of 10 nT, while B_x rarely (less than $\sim 0.001\%$ of the
 369 time per each bin) falls outside the range of -10 nT $\leq B_x \leq +10$ nT. The positive
 370 offset in the north/south component of the field is still apparent within the central plasma
 371 sheet, as is the aberration of the magnetotail, albeit to a lesser amount within the sheet
 372 compared to within the lobes (cf. panels 3g and 3j).

Figure 4 displays the distribution of the magnetic field components within the mag-
 374 netotail measured by ARTEMIS as a function of electron number density for the same
 375 conditions as in Figure 3; i.e., (a–c) all observations, (d–f) sheath-like conditions, (g–i)
 376 lobe-like conditions, and (j–l) sheet-like conditions. For these, we do not include mea-
 377 surements of densities below $n < 0.03$ cm $^{-3}$, to ensure accurate calculations of the ion
 378

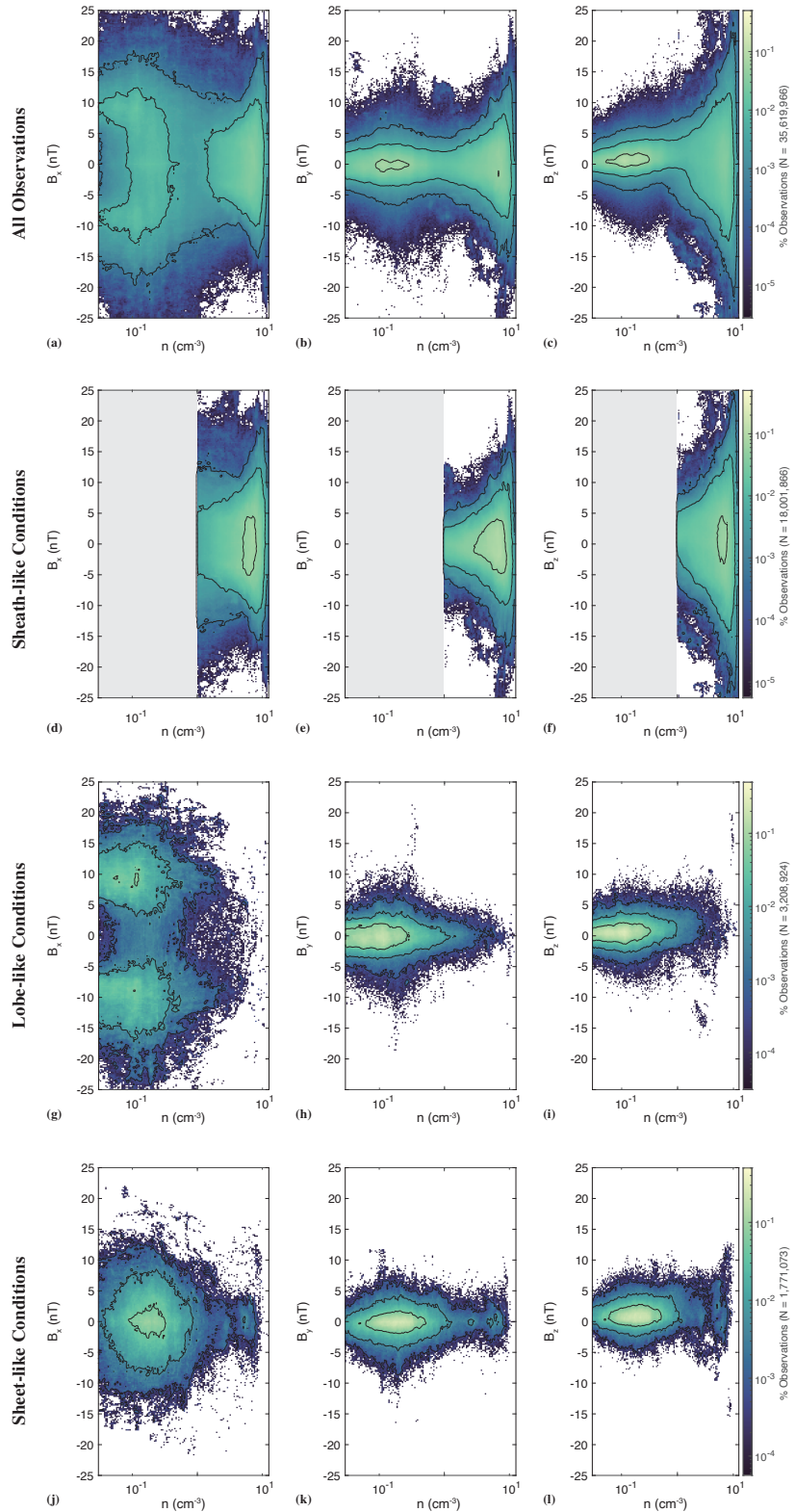


Figure 4. Heatmaps displaying magnetic field components as a function of electron number density for the same magnetotail conditions as displayed in Figure 3. Instrument counts corresponding to densities below 0.03 cm^{-3} are excluded to ensure an accurate density calculation.

379 moments which become unreliable when ARTEMIS detects too few geophysical parti-
 380 cle counts (McFadden, Carlson, Larson, Bonnell, et al., 2008; Poppe, 2019); recall that
 381 this is automatically satisfied for sheath-like conditions since we require $n \geq 1 \text{ cm}^{-3}$.
 382 Note that a population of even lower-density plasma may at times be present within the
 383 lobes of the magnetotail that is “hidden” from the ARTEMIS probes when exposed to
 384 sunlight (see Liuzzo, Poppe, et al., 2021), the effect of which is not included in this anal-
 385 ysis. Due to this additional requirement on the plasma density, the number of observa-
 386 tions used to generate the heatmaps in each row of Figure 4 is reduced compared to Fig-
 387 ure 3 by as much as 21%.

388 The top row of Figure 4 highlights a distinct correlation between the density and
 389 magnetic field components. Within the magnetotail, Panels 4b and 4c show that the am-
 390 bient magnetospheric density near the lunar orbit is most frequently centered near a value
 391 of $n \approx 0.2 \text{ cm}^{-3}$, correlated with minima in $|B_y|$ and $|B_z|$. For nearly all observations
 392 with densities $n \lesssim 0.2 \text{ cm}^{-3}$, B_y and B_z remain within approximately $\pm 15 \text{ nT}$. For the
 393 B_x component, the peak in ARTEMIS observations near a density of $n \approx 0.2 \text{ cm}^{-3}$ is
 394 much more extended compared to the other two components, nearly evenly distributed
 395 for all values within $|B_x| \lesssim 10 \text{ nT}$. With increasing densities, however, the magnitudes
 396 of each field component extend to successively larger values. At densities beyond $n \gtrsim$
 397 1 cm^{-3} , all three components reach values up to approximately $\pm 15 \text{ nT}$ at a frequency
 398 that is nearly evenly distributed, with $|B_x|$ and $|B_z|$ reaching maxima beyond 25 nT . This
 399 feature marks the ARTEMIS probes’ encounters with the edge of the terrestrial mag-
 400 netosheath: as also visible in Figures 4d–4f, the densities for sheath-like conditions peak
 401 near a value of 8 cm^{-3} with a broad spread in each component of the magnetic field (see
 402 also Figures 3d–3f).

403 Figures 4g–4i further confirm that the higher-density plasma is associated with the
 404 lunar passage through the magnetosheath: the ambient plasma density within the lobes
 405 of the terrestrial magnetotail near the lunar orbit rarely exceeds a value of 1 cm^{-3} . Rather,
 406 the contour denoting the most frequent observations illustrates that the tenuous lobe-
 407 like plasma reaches densities as low as $n = 0.03 \text{ cm}^{-3}$ (i.e., the ARTEMIS ESA detec-
 408 tion limit considered for this study) and extends to values an order of magnitude larger
 409 with $n \approx 0.3 \text{ cm}^{-3}$. The structure of the magnetic field within the lobes is also clearly
 410 visible in panels 4g–4i. In B_x , a bifurcated signature forms near a density of $n = 0.1$
 411 cm^{-3} , with the maxima in observations centered near $B_x = \pm 10 \text{ nT}$. Conversely, the

⁴¹² B_y and B_z components remain near a value of 0 nT, with the largest number of obser-
⁴¹³ vations between $-2 \text{ nT} < B_y, B_z < 2 \text{ nT}$; nearly every lobe-like measurement of these
⁴¹⁴ components remained within $\pm 10 \text{ nT}$ over the course of the ten-year data set.

⁴¹⁵ For sheet-like conditions, Figures 4j–4l illustrate that the densities observed by ARTEMIS
⁴¹⁶ are, on average, shifted to slightly larger values than in the magnetotail lobes: the inner-
⁴¹⁷ most contour in each panel now encompasses values from $0.08 \text{ cm}^{-3} < n < 0.7 \text{ cm}^{-3}$,
⁴¹⁸ nearly three times higher than in the lobes. As also seen in Figures 3j–3l, the magnetic
⁴¹⁹ field within the sheet is reduced in magnitude, with B_x and B_y centered around 0 nT
⁴²⁰ and an overall positive shift in B_z (see also Behannon, 1970).

⁴²¹ 3.2 Properties of the plasma velocity

⁴²² Figure 5 displays heatmaps for the ARTEMIS measurements of the bulk plasma
⁴²³ velocity components within the terrestrial magnetotail, in the same layout as Figure 3.
⁴²⁴ The top row (5a–5c) includes all ten years of observations, whereas the lower three rows
⁴²⁵ separate the data into (5d–5f) magnetosheath-like, (5g–5i) magnetotail lobe-like, and (5j–
⁴²⁶ 5l) sheet-like conditions, respectively. To ensure accuracy in the velocity moment, we only
⁴²⁷ calculate velocities using instrument counts that correspond to number densities of $n >$
⁴²⁸ 0.03 cm^{-3} in Figure 5 (as also consistent with Figure 4). The observations of the velo-
⁴²⁹ city components are accumulated into linearly-spaced bins with a width and height of ap-
⁴³⁰ proximately 3 km/s.

⁴³¹ Figures 5a and 5b highlight that the V_x component of the flow is shifted notice-
⁴³² ably tailward (i.e., $V_x < 0$), with a median value of $V_x = -240 \text{ km/s}$. The distribu-
⁴³³ tion of V_x in the magnetotail is bimodal, with the most frequent observations peaking
⁴³⁴ near values of $V_x \approx 0 \text{ km/s}$ and $V_x \approx -400 \text{ km/s}$. For the former, the V_y component
⁴³⁵ of the bulk plasma velocity remains near a value of $\sim 0 \text{ km/s}$, with speeds that only rarely
⁴³⁶ extend beyond 100 km/s. For the latter, however, V_y displays a distinct divergence to
⁴³⁷ large velocities for the most negative values of V_x (i.e., for the fastest tailward flows),
⁴³⁸ frequently reaching speeds approaching $|V_y| \approx 200 \text{ km/s}$. The V_z component of the mag-
⁴³⁹ netotail flow, on the other hand, displays only a narrow, symmetric spread about its mean
⁴⁴⁰ value of $V_z \approx 0 \text{ km/s}$ and rarely exceeds 200 km/s, with most commonly observed ve-
⁴⁴¹ locities of $|V_z| \lesssim 25 \text{ km/s}$.

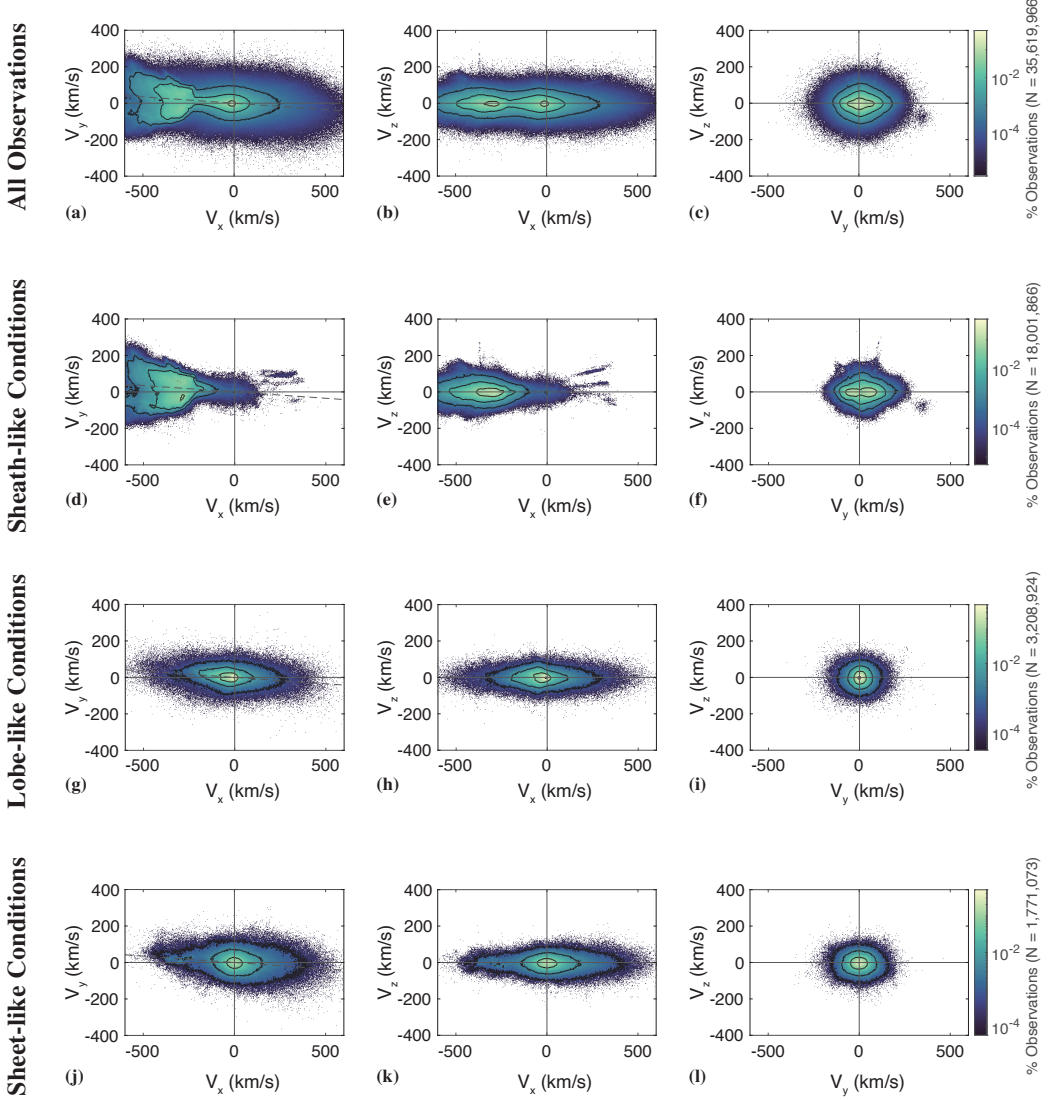


Figure 5. Identical to Figure 3, but for the components of the bulk plasma velocity. Note that velocities calculated using instrument counts that correspond to number densities of $n < 0.03 \text{ cm}^{-3}$ are excluded from the data set.

Figures 5d–5f illustrate that the divergent behavior in V_y is driven by the flow within the terrestrial magnetosheath. After encountering the Earth's magnetic field, shocked solar wind plasma is diverted and imparts a strong component to the flow directed away from the planet (i.e., resulting in a $\pm V_y$). The signature of the aberrated tail is also visible, with the V_y component symmetric about the dashed line in panel 5d corresponding to a 4° tilt. These panels also show that the magnetosheath flows are almost entirely tailward, with a mean value of V_x exceeding -300 km/s . Note that the limited obser-

449 vations suggesting $V_x > 0$ velocities (for less than 0.001% per bin; see panels 5d and
 450 5e) may satisfy the requirements for sheath-like conditions described above but are likely
 451 *not* associated with Earthward magnetosheath flows.

452 For lobe-like conditions, Figures 5g–5i show that each velocity component is more
 453 narrowly distributed compared to the whole data set. In V_y and V_z , nearly all observa-
 454 tions occur with $-100 \text{ km/s} < V_y, V_z < +100 \text{ km/s}$. Panel 5i illustrates that these com-
 455 ponents are nearly isotropic, and were most frequently observed (at more than 1% of the
 456 time per bin) between values of $-9 \text{ km/s} < V_y < +6 \text{ km/s}$ and $-9 \text{ km/s} < V_z < +3$
 457 km/s . ARTEMIS detected V_x flows that were most frequently shifted anti-Earthward
 458 (i.e., $V_x < 0$) within the lobes, with the peak in measurements located between -100
 459 $\text{km/s} < V_x < 20 \text{ km/s}$ (see panel 5g). Despite this tailward offset at lower velocities,
 460 the distribution for cases with $|V_x| \gtrsim 250 \text{ km/s}$ is remarkably symmetric (see Figures
 461 5g and 5h), with considerable Earthward *and* anti-Earthward flows for these lobe-like
 462 conditions. These somewhat frequent, high-velocity measurements are likely signatures
 463 of reconnection events within the tail: the Earthward velocities suggest a translunar X-
 464 line well down-tail of the ARTEMIS probes (e.g., Slavin et al., 1985; Kiehas et al., 2018),
 465 while the anti-Earthward velocities—suggesting cislunar reconnection—emphasize the
 466 variability in the location of the tail reconnection region. As a result, these signatures
 467 frequently pass ARTEMIS located near $60R_E$ downstream of the planet, resulting in both
 468 Earthward *and* tailward velocities being observed by the probes (see also Figure 1 and
 469 Artemyev, Angelopoulos, Runov, & Vasko, 2017; Wang et al., 2020).

470 For plasma sheet-like conditions, the bottom row of Figure 5 still illustrates a broad
 471 spread in V_x at velocities exceeding $|V_x| > 250 \text{ km/s}$, likely signatures of magnetotail
 472 reconnection events. However, all three components were more commonly observed at
 473 lower values: the most frequent measurements were obtained with $-50 \text{ km/s} < V_x, V_y, V_z <$
 474 50 km/s . Hence, compared to flows within the magnetotail lobes, the peak in the dis-
 475 tribution of the velocity components observed within the plasma sheet are more sym-
 476 metric around 0 km/s, especially along the x direction.

477 Figure 6 displays the components of the plasma bulk velocity as a function of elec-
 478 tron number density as observed by ARTEMIS within the magnetotail, following the lay-
 479 out of the previous three figures. As with the magnetic field (see Figure 4), there is a
 480 distinct correlation between the flow velocity and number density. For the whole set of

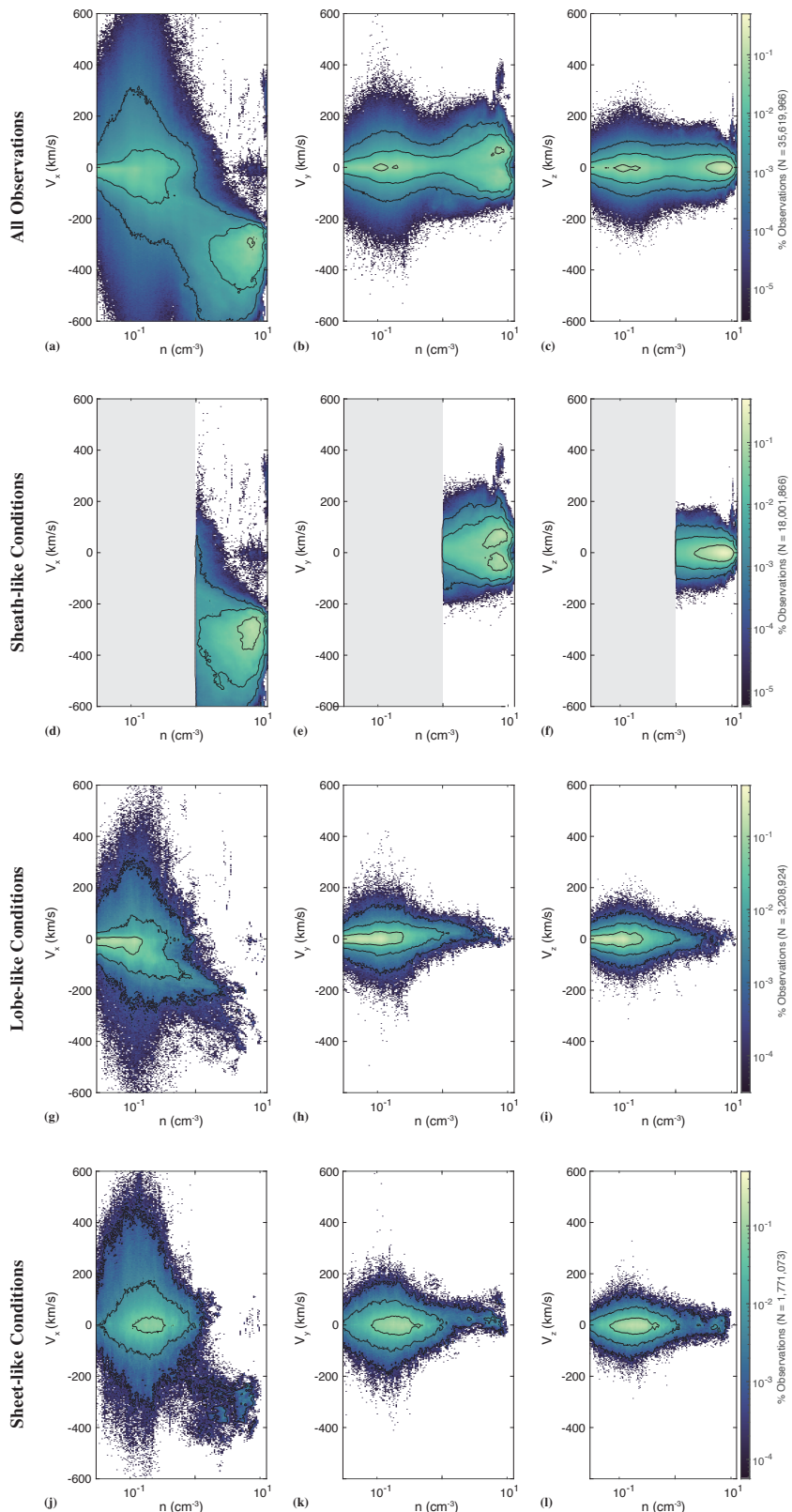


Figure 6. Identical to Figure 4, but for the components of the plasma bulk velocity as a function of number density.

481 observations (panels 6a–6c), each velocity component has two separate regions corresponding
 482 to peaks in the observations. One of these is located at low densities centered near
 483 $n \approx 0.1 \text{ cm}^{-3}$, with panels 6b and 6c showing that the most frequent observations oc-
 484 curred with $0.03 \text{ cm}^{-3} < n < 0.5 \text{ cm}^{-3}$. As also visible in Figure 5, this peak spans
 485 a broad range of V_x values extending beyond $|V_x| \geq 300 \text{ km/s}$, but is narrower in V_y
 486 and V_z . The second enhancement is located at higher densities ($n > 5 \text{ cm}^{-3}$), centered
 487 near a value of $n \approx 8 \text{ cm}^{-3}$. Notably, this high-density enhancement is associated with
 488 strong tailward velocities of $V_x \approx -300 \text{ km/s}$ (see panel 6a) and a bifurcation in V_y .
 489 As visible in panels 6d–6f, this second peak is indicative of the probes' passage through
 490 the magnetosheath plasma (see also Figure 5).

491 Comparing the bottom two rows of Figure 6 highlights the differences between the
 492 plasma environment within the magnetotail lobes and plasma sheet. Specifically, lobe-
 493 like conditions are, most frequently, associated with a more tenuous plasma with $n \lesssim$
 494 0.2 cm^{-3} , while sheet-like conditions are associated with a denser plasma with $n \gtrsim 0.2$
 495 cm^{-3} (cf. panels 6g–6i with panels 6j–6l). Note that despite the filtering for lobe-like and
 496 sheet-like conditions, a small amount of magnetosheath-like plasma ($\lesssim 0.01\%$ per bin)
 497 is still present for these regions, especially visible at high densities ($n > 1 \text{ cm}^{-3}$) and
 498 strong tailward velocities ($V_x \ll 0$). As also seen in Figure 5, panel 6g illustrates that
 499 the signature of reconnection outflow is visible in the data even for lobe-like conditions,
 500 with Earthward and tailward velocities reaching $|V_x| \approx 500 \text{ km/s}$.

501 While similar high-velocity flows are also present in panel 6j for magnetotail plasma
 502 sheet-like fields (see also Figure 5), they are more often directed Earthward (with flows
 503 reaching values up to $V_x = +600 \text{ km/s}$) than they are tailward (with flows that rarely
 504 exceed $V_x = -400 \text{ km/s}$). This may suggest reconnection regions within the plasma
 505 sheet that are more frequently located tailward of the Moon. Such a finding is consis-
 506 tent with Slavin et al. (1985), who found that the location of the down-tail reconnection
 507 region was on average located $120R_E$ – $140R_E$ downstream of the Earth during the ISEE-
 508 3 magnetotail encounters. This result also agrees with the study by Kiehas et al. (2018),
 509 who used data from the first five years of the ARTEMIS mission and found that a large
 510 fraction (43%–56%) of the reconnection-related flows detected within the magnetotail
 511 plasma sheet were directed Earthward. However, the large spread in V_x visible in Fig-
 512 ure 6j—reaching large values both Earthward *and* tailward—again suggests a highly vari-
 513 able location to the neutral line (see also Kiehas et al., 2018).

514 **3.3 Statistics of the lunar plasma environment within the magnetotail**

515 Figure 7 displays overlapping histograms of (a) components of the magnetic field,
 516 (b) components of the bulk plasma velocity, and (c) plasma number density, ion tem-
 517 perature, ion and electron temperature ratio, and ion specific entropy for the same four
 518 scenarios in the previous figures: (black, outlined) all ARTEMIS observations within the
 519 magnetotail, (blue, filled) magnetosheath-like conditions, (green, filled) magnetotail lobe-
 520 like conditions, and (red, filled) plasma sheet-like conditions. Here, the ion specific en-
 521 tropy s_i is proportional to the ratio between the ion plasma pressure p_i and the num-
 522 ber density ($s_i \propto p_i/n_i^\gamma$; see, e.g., Goertz & Baumjohann, 1991; Borovsky et al., 1998;
 523 Wing et al., 2014). For each of the conditions, we assume that the plasma is isotropic
 524 with polytropic index $\gamma = 5/3$ for simplicity (e.g., Baumjohann, 1993). The histograms
 525 in Figure 7 are normalized by the total number of observations for each respective sce-
 526 nario (i.e., the values of N as provided in Figure 3 for the magnetic field or in Figure 5
 527 for the plasma moments). Again, note that for measurements of the plasma moments
 528 in panels 7b and 7c, we require sufficient ARTEMIS instrument counts corresponding
 529 to an ambient density of $n > 0.03 \text{ cm}^{-3}$. The magnetic field histograms in panel 7a are
 530 accumulated into bins that are 2 nT wide, panel 7b uses a 20 km/s bin width for the ve-
 531 locity, and the bins for temperature in panel 7c are 25 eV wide. The bin widths for the
 532 number density, temperature ratio, and entropy each increase logarithmically: for den-
 533 sity, the bins increase from a width of $4.26 \cdot 10^{-3} \text{ cm}^{-3}$ at the lowest densities to a bin
 534 width of 2.49 cm^{-3} at the highest densities, for the temperature ratio, the bins increase
 535 from widths of 0.05 to 4.50, and for specific entropy, the bins increase from $1.27 \cdot 10^{-4}$
 536 nPa cm⁵ in width to 0.84 nPa cm⁵. Besides the normalized histograms, each panel in
 537 Figure 7 includes the median value for each quantity, represented by vertical dashed lines,
 538 as well as the standard deviation above and below the median, represented by horizon-
 539 tal lines along the top of each panel. Additional statistical parameters for these quan-
 540 tities can be found in Table 1.

541 Figure 7a shows that the B_y and B_z components of the magnetic field within the
 542 magnetotail lobes and plasma sheet are similar, peaking near 0 nT for each of the sep-
 543 arate regions that rapidly decrease at larger magnitudes. Notably, the histogram for B_z
 544 is clearly shifted toward positive values for each of the magnetotail locations, with the
 545 median value near the central plasma sheet (0.97 nT) nearly a factor of two larger than
 546 in the lobes (0.51 nT). Again, this overall shift of $B_z > 0$ is indicative of the orienta-

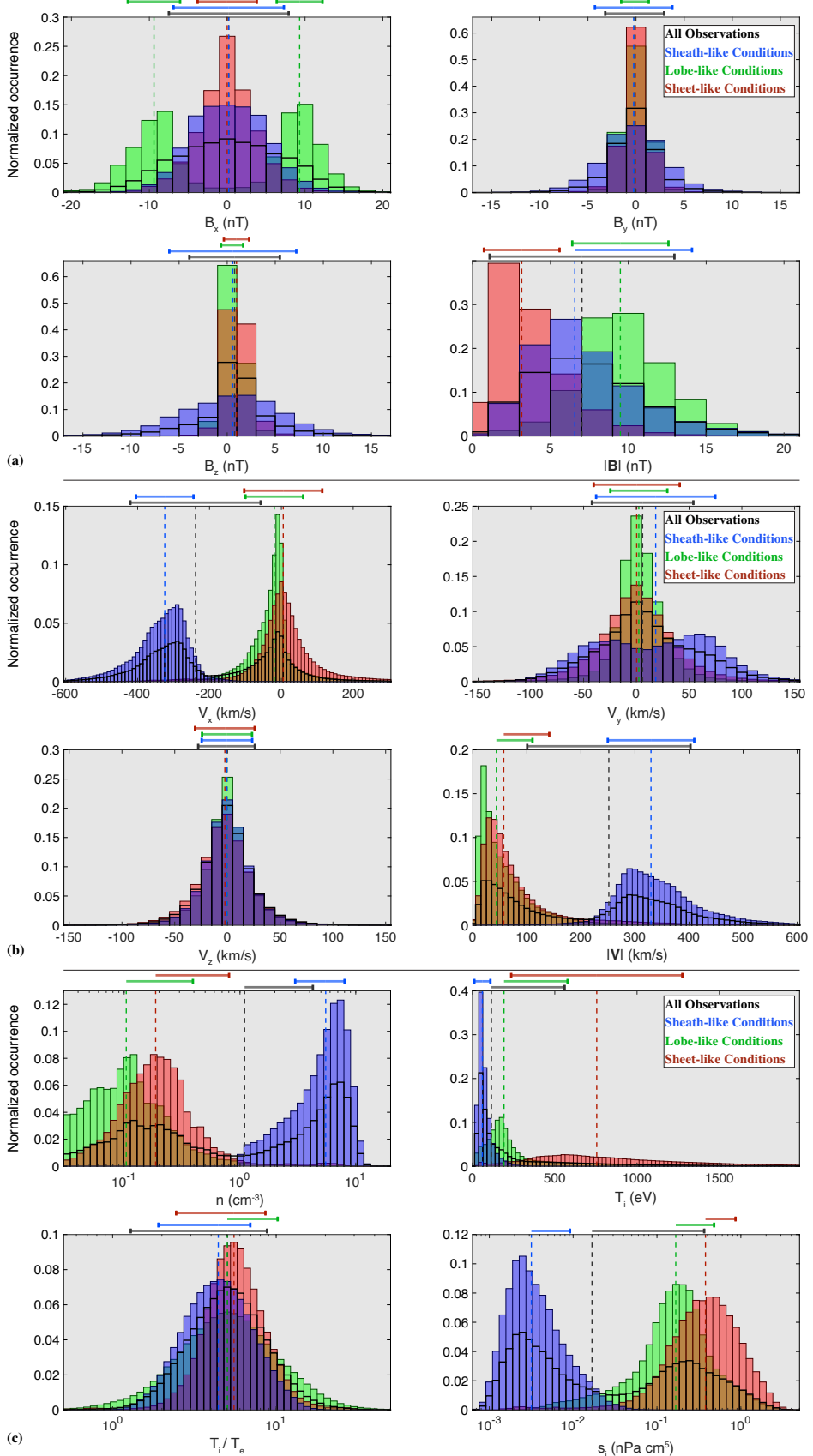


Figure 7. Overlapping histograms of the (a) magnetic field (b) bulk plasma velocity, and (c) plasma number density, ion temperature, ion and electron temperature ratio, and ion specific entropy as observed by ARTEMIS for (black, outlined) all conditions, (blue, filled) magnetosheath-like conditions only, (green, filled) lobe-like conditions only, and (red, filled) plasma sheet-like conditions only. Each panel is normalized by the number of observations for the respective magnetotail condition. For each condition, dashed vertical lines represent the median value of the respective quantity, while horizontal bars at the top of each panel denote the standard deviation, centered at the median value (see Table 1 for relevant parameters). Note that standard deviations below the median value are not included for cases that would result in a negative magnitude, density, temperature, or entropy.

tion of the magnetospheric field near the lunar orbit (as is also visible in, e.g., Figure 3 and Table 1). Within the magnetosheath, the B_y and B_z components are similarly centered near zero (with a slightly positive shift in B_z), but their distributions are much broader compared to within the lobes or plasma sheet.

Despite similarities in B_y and B_z for magnetotail lobe-like and sheet-like conditions, the differences in the field configurations for these two scenarios become visible in B_x and $|\mathbf{B}|$. In B_x , the histograms for the northern and southern lobes are bimodal, nearly following two normal distributions centered around ± 10 nT, with standard deviations of nearly 3 nT. Within the sheet, while the spread of B_x is similar as in each of the lobes, the distribution is much more focused near $B_x \approx 0$ nT than in the lobes. The magnetosheath field is also nearly centered around 0 nT, but with a distribution that is again much broader than that of the sheet-like fields. The magnetic field magnitude is noticeably different between each of these magnetotail regions as well. The median value of $|\mathbf{B}| = 3.16$ nT is at its smallest within the plasma sheet and is more than two times lower than the median within the magnetosheath of $|\mathbf{B}| = 6.53$ nT, which itself is nearly 1.5 times lower than the median value of $|\mathbf{B}| = 9.48$ nT within the magnetotail lobes. The weakened field magnitude within the plasma sheet is a characteristic feature of the magnetotail, coinciding with the passage through the neutral region of the magnetotail field (e.g., Bame et al., 1967).

Figure 7b shows the velocity distribution; for lobe- and sheet-like conditions (green and red, respectively, in Figure 7b), the V_x components are approximately symmetric about $V_x = 0$ km/s. However, the distribution is shifted tailward for lobe-like conditions (with a median value of $V_x = -20$ km/s), while the sheet-like distribution is shifted slightly Earthward (with a median of $V_x = +4$ km/s). In comparison, the magnetosheath flow is decidedly tailward, with a median value of $V_x = -324$ km/s and tailward speeds that only rarely drop below 200 km/s. In V_y , the lobe-like and sheet-like distributions are similar, nearly symmetric around $V_y = 0$ km/s, with the distribution of the lobe-like flows more narrowly peaked than for sheet-like conditions. The deflected plasma flow within the magnetosheath is especially visible in this figure, with a bimodal distribution in V_y consisting of peaks located near -30 km/s and $+60$ km/s (i.e., slightly biased toward the $+\hat{\mathbf{y}}$ direction). Notably, measurements with $V_y > +100$ km/s (i.e., within the dusk flank of the magnetosheath) occur more frequently than those with $V_y < 100$ km/s (i.e., within the dawn flank). These asymmetries are signatures of the aberration in the

580 magnetotail at the lunar orbit, as was also visible in Figure 5d. The distribution of the
 581 V_z component is nearly independent of the location of the probes within the magneto-
 582 tail; instead, the north/south component of the flow always follows a quasi-normal dis-
 583 tribution that is centered near $V_z = 0$ km/s.

584 Figure 7c shows normalized histograms for the electron number density and plasma
 585 temperature in the magnetotail. As also visible in Figures 4 and 6, the densities are, on
 586 average, lower in the lobes than the plasma sheet, with a slight overlap near a value of
 587 $n \approx 0.2$ cm $^{-3}$. These, however, are each dwarfed by the densities within the magne-
 588 tosheath which peak at over an order of magnitude larger, near values of $n \approx 8$ cm $^{-3}$.
 589 Panel 7c illustrates a stark difference in the plasma temperatures for these separate mag-
 590 netotail plasma conditions as well, with the coldest population within the magnetosheath
 591 (with median temperatures of $T_e = 14$ eV and $T_i = 60$ eV), followed by the warmer
 592 magnetotail lobes (with medians of $T_e = 39$ eV and $T_i = 190$ eV) compared to the
 593 warmest plasma within the sheet (with medians $T_e = 132$ eV and $T_i = 733$ eV). For
 594 this warmest population, the distribution has a long tail that extends to temperatures
 595 beyond 2000 eV within the sheet. Using the average values for number density, temper-
 596 ature, and magnetic field strength in Table 1, we find that the magnetotail lobe-like con-
 597 ditions are in pressure balance with the plasma sheet-like conditions to within $\sim 10\%$
 598 (see also Matsumoto et al., 2001). This minor difference may be due to the presence of
 599 particles within the plasma sheet that exceed the energy range observable by the ARTEMIS
 600 Solid State Telescope (e.g., Sarris et al., 1981; Angelopoulos, 2008).

601 Figure 7 also illustrates that the mean value for the ratio between the ion and elec-
 602 tron temperatures is near 5 for all scenarios studied (see also Table 1). The distribution
 603 of this ratio for lobe-like conditions (with median value $T_i/T_e = 5.52$) is narrower than
 604 those of the sheath-like (median $T_i/T_e = 4.96$) or lobe-like populations (median $T_i/T_e =$
 605 5.02). The average values for the ion and electron temperature ratios near the lunar dis-
 606 tance of $60R_E$ are consistent with the measurements within the near-Earth magnetotail
 607 (see, e.g., Lavraud et al., 2009; Wang et al., 2012; Wing et al., 2014; Grigorenko et al.,
 608 2016). However, the ARTEMIS observations reach values that extend beyond the range
 609 of T_i/T_e observed closer to Earth—especially within the lobes where T_i/T_e even drops
 610 below 1. Also visible in Figure 7 is a clear separation in the specific entropy of the ions.
 611 As is the case closer to Earth, (see, e.g., Wing et al., 2014), s_i within the magnetosheath
 612 is, on average, 2–3 orders of magnitude below the value within the magnetotail plasma

sheet near the Moon's orbital position. For lobe-like conditions, the ion specific entropy is (on average) slightly reduced compared to the plasma sheet, but at times reaches values similar to those observed within the magnetosheath due to the substantial spread of the entropy distribution.

Table 1: Statistical parameters for the magnetic field, plasma flow velocity, number density, ion and electron temperature, ion and electron temperature ratio, and ion specific entropy with the Moon located within Earth's magnetotail. Shown are the standard deviation (σ), mean (μ), median (Me), mode (Mo), Pearson kurtosis (K), and skewness (Sk) for the range of the ARTEMIS observations as displayed in Figure 7. Note that the modes are rounded to the nearest integer, except for the number density, temperature ratio, and specific entropy.

Magnetic Field (nT)	σ	μ	Me	Mo	K	Sk
B_x : All	6.73	0.17	0.20	0	2.56	-0.05
B_x : Sheath-like	4.81	0.27	0.19	0	3.22	0.12
B_x : Lobe-like (N)	2.90	9.33	9.30	9	4.02	0.00
B_x : Lobe-like (S)	3.17	-9.66	-9.38	-9	3.70	-0.17
B_x : Sheet-like	3.79	-0.05	0.00	0	4.08	-0.05
B_y : All	2.67	-0.17	-0.14	0	6.18	-0.10
B_y : Sheath-like	3.41	-0.25	-0.25	0	4.30	-0.05
B_y : Lobe-like	1.43	-0.08	-0.11	0	7.26	-0.04
B_y : Sheet-like	1.46	-0.08	-0.07	0	7.46	-0.21
B_z : All	3.81	0.65	0.77	1	5.78	-0.31
B_z : Sheath-like	5.28	0.37	0.58	1	3.18	-0.10
B_z : Lobe-like	1.15	0.56	0.51	0	10.6	0.12
B_z : Sheet-like	1.32	1.08	0.97	1	8.21	0.47
$ \mathbf{B} $: All	3.63	7.35	7.00	6	3.30	0.61
$ \mathbf{B} $: Sheath-like	3.46	7.12	6.53	6	4.02	0.94
$ \mathbf{B} $: Lobe-like	2.95	9.70	9.48	9	3.72	0.27
$ \mathbf{B} $: Sheet-like	2.41	3.68	3.16	2	5.64	1.34
Velocity (km/s)	σ	μ	Me	Mo	K	Sk
V_x : All	175	-189	-240	-8	1.97	0.12

V_x : Sheath-like	77.6	-335	-324	-288	5.29	-0.28
V_x : Lobe-like	73.1	-30.0	-19.8	-7	10.6	-0.83
V_x : Sheet-like	95.2	3.99	4.15	-1	7.40	-0.82
V_y : All	46.1	9.28	5.83	0	3.14	0.14
V_y : Sheath-like	55.1	15.2	17.9	63	2.18	-0.04
V_y : Lobe-like	25.1	3.69	2.37	1	8.09	0.06
V_y : Sheet-like	37.9	0.67	0.37	0	4.49	0.04
V_z : All	26.4	-0.81	-0.90	-1	5.76	0.06
V_z : Sheath-like	23.8	-0.13	-0.50	-1	5.64	0.20
V_z : Lobe-like	23.2	-0.21	-0.40	0	6.73	0.00
V_z : Sheet-like	27.7	-2.84	-2.46	-1	5.41	-0.03
$ \mathbf{V} $: All	149	218	251	23	1.81	0.14
$ \mathbf{V} $: Sheath-like	77.1	340	329	293	4.06	0.52
$ \mathbf{V} $: Lobe-like	64.2	63.9	43.4	18	14.7	2.82
$ \mathbf{V} $: Sheet-like	83.0	85.3	57.1	35	9.15	2.32

Number Density (cm^{-3})	σ	μ	Me	Mo	K	Sk
n : All	3.16	2.86	1.10	0.11	2.25	0.78
n : Sheath-like	2.50	5.44	5.50	6.94	2.19	0.10
n : Lobe-like	0.29	0.16	0.10	0.05	258	12.5
n : Sheet-like	0.62	0.30	0.19	0.14	81.0	8.25

Ion Temperature (eV)	σ	μ	Me	Mo	K	Sk
T_i : All	379	290	112	41	6.93	2.07
T_i : Sheath-like	47.6	72.6	59.7	41	93.3	5.15
T_i : Lobe-like	328	311	190	174	9.03	2.39
T_i : Sheet-like	429	807	733	557	2.76	0.59

Electron Temperature (eV)	σ	μ	Me	Mo	K	Sk
T_e : All	96.6	59.1	20.9	13	30.6	4.25
T_e : Sheath-like	9.67	15.3	14.3	13	7027	56.9
T_e : Lobe-like	91.4	66.8	39.3	31	41.1	4.93
T_e : Sheet-like	144	172	132	74	13.2	2.48

Temperature Ratio	σ	μ	Me	Mo	K	Sk
T_i/T_e : All	3.63	5.86	5.04	3.68	15.5	2.51
T_i/T_e : Sheath-like	2.48	4.96	4.42	3.51	6.56	1.39
T_i/T_e : Lobe-like	4.91	6.34	5.02	2.98	12.4	2.41
T_i/T_e : Sheet-like	3.06	6.12	5.52	4.77	17.7	2.65

Specific Entropy (nPa cm⁵)	σ	μ	Me	Mo	K	Sk
s_i : All	0.348	0.183	0.017	0.0019	18.9	3.42
s_i : Sheath-like	0.006	0.005	0.003	0.0019	207	7.75
s_i : Lobe-like	0.312	0.257	0.168	0.0974	21.7	3.58
s_i : Sheet-like	0.485	0.528	0.379	0.0021	8.17	1.97

4 Discussion and Conclusions

Using more than ten years of data from the ARTEMIS mission in orbit around the Moon, this study has investigated the properties of the terrestrial magnetotail plasma environment at distances of approximately $60R_E$ downstream of Earth. When located within Earth's down-tail magnetosphere, the lunar plasma environment is highly variable, depending on its location within the magnetotail. Lobe-like fields result in a low-density plasma environment with an approximately 10 nT field and range of plasma flow velocities, sheet-like conditions yield a weaker field magnitude and denser plasma population, and magnetosheath-like conditions are characterized by the highest densities with intermediate magnetic fields and a rapid tailward flow. Our findings can be briefly summarized as follows:

- During a typical crossing of the terrestrial magnetotail, the Moon experiences a wide range of plasma environments. These disparate regions of the down-tail magnetosphere can, to first order, be grouped into magnetosheath-like, magnetotail lobe-like, and magnetotail plasma sheet-like conditions. However, there are multiple small-scale events (including signatures of reconnection) that occur within these regions of the magnetotail, causing the local lunar plasma environment to deviate from these more general characterizations.
- For magnetotail lobe-like conditions, the magnetic field magnitude peaks near a value of 10 nT and is almost entirely aligned with the Earthward/anti-Earthward

637 B_x component; the values of B_y and B_z are centered near 0 nT. Near the central
 638 plasma sheet, the magnetic field minimizes in all three components, with an av-
 639 erage magnitude below 4 nT. The field within the magnetosheath is more broadly
 640 distributed compared to within the lobes or plasma sheet, with an intermediate
 641 magnitude compared to the other two locations. For all of the observations in the
 642 tail, the north/south component of the field is, on average, shifted by 1–2 nT to
 643 slightly positive values, a signature of the orientation of Earth’s magnetic field.
 644 The $\sim 4^\circ$ aberration of the magnetotail is also clearly visible in the magnetic field
 645 when comparing the distribution of the B_x and B_y components.

- 646 • Bulk flow velocities are preferentially directed anti-Earthward in the tail, especially
 647 within the magnetosheath and for the most frequent observations within the lobes,
 648 but this preference is reduced in the plasma sheet. Rapid Earthward and anti-Earthward
 649 plasma flows are, at times, detected near the Moon (even when located within the
 650 magnetotail lobes), which likely indicate variability in the location of the tail re-
 651 connection region.
- 652 • Plasma number densities vary by more than an order of magnitude near the Moon
 653 when located in the magnetotail, but the low-density lobes, intermediate-density
 654 sheet, and high-density magnetosheath are each clearly distinguishable. Plasma
 655 temperatures are also well-separated within the magnetotail, with the magnetosheath
 656 plasma much cooler than the lobes, which is cooler than the extended tail to the
 657 distribution of the temperatures within the central plasma sheet.

658 To illustrate the variability of the lunar magnetotail plasma environment in a dif-
 659 ferent manner, Figure 8 displays heatmaps of the Alfvénic Mach number as a function
 660 of plasma beta. The panels display these quantities for the conditions defined in section
 661 3: (a) all ARTEMIS observations over the ten-year mission, (b) magnetosheath-like con-
 662 ditions only, (c) magnetotail lobe-like conditions only, and (d) magnetotail plasma sheet-
 663 like conditions only. As visible in panel 8a, the Alfvénic Mach number of the ambient
 664 magnetotail plasma spans multiple orders of magnitude near the Moon’s orbit, ranging
 665 from decidedly sub-Alfvénic with $M_A < 10^{-3}$ to super-Alfvénic conditions with $M_A >$
 666 10^2 . Similarly, the plasma beta displays a variability of nearly five orders of magnitude,
 667 from $10^{-2} \leq \beta \leq 10^3$, and shows a generally positive correlation with the Alfvénic
 668 Mach number. Panel 8b illustrates that the fast flows and enhanced densities of the mag-
 669 netosheath population are responsible for the extrema in the values of the Alfvénic Mach

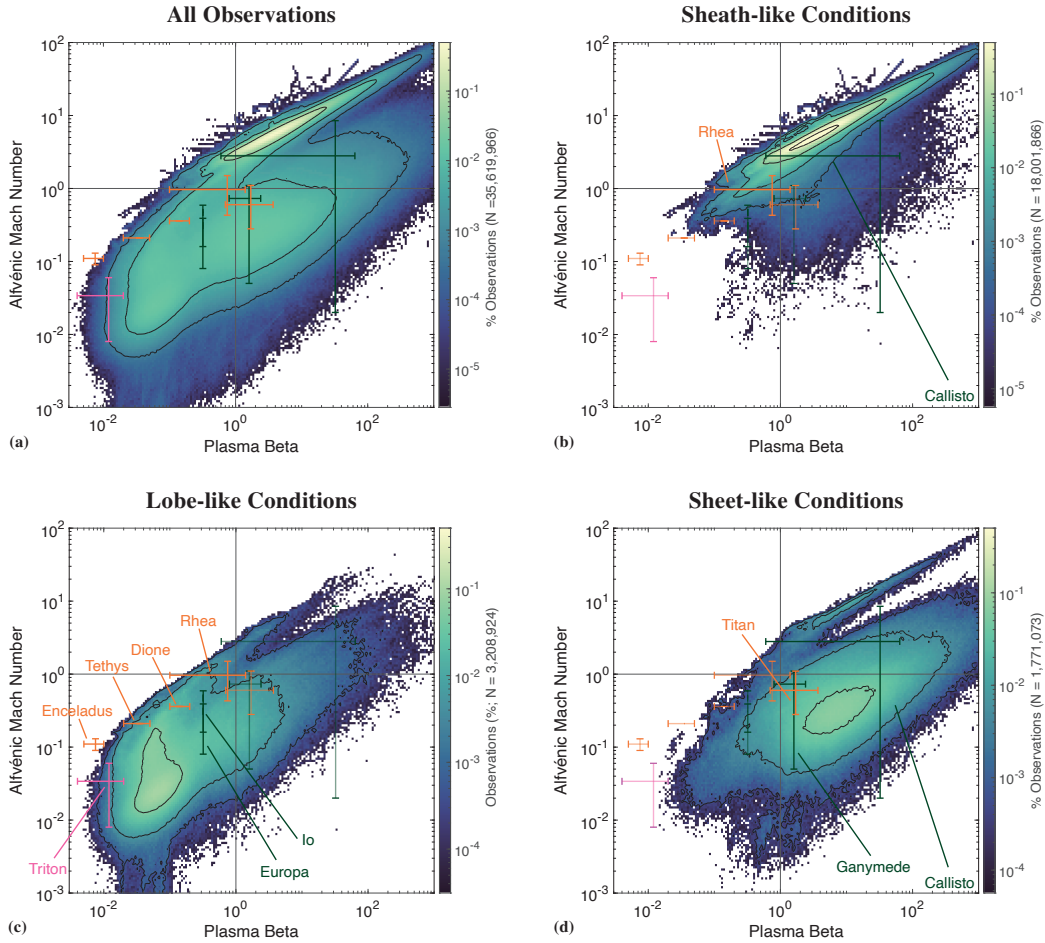


Figure 8. Heatmaps of the Alfvénic Mach number as a function of plasma beta observed by ARTEMIS when located within Earth’s magnetotail for (a) all conditions, (b) magnetosheath-like conditions, (c) magnetotail lobe-like conditions, and (d) magnetotail plasma sheet-like conditions. Overplot are ranges of M_A and β experienced by select moons of (dark green) Jupiter, (orange) Saturn, and (pink) Neptune’s moon Triton.

number and plasma beta in panel 8a, visible as a thin ridge extending to the largest values of M_A and β . Comparison of panels 8c and 8d highlight that the lobe-like plasma has, on average, a lower Alfvénic Mach number and plasma beta (with median values of $M_A = 0.07$ and $\beta = 0.09$) than near the magnetotail plasma sheet (with median values of $M_A = 0.39$ and $\beta = 7.29$).

To place the variability of the lunar plasma environment in the context of the plasma environments near various other moons throughout the solar system, Figure 8 also includes ranges of Alfvénic Mach numbers and plasma betas experienced by select outer-

678 planet moons during their orbits around their parent planets. Displayed are ranges in
 679 M_A and β for the four Galilean moons of Jupiter in dark green, five moons of Saturn
 680 (Enceladus, Tethys, Dione, Rhea, and Titan) in orange, and Neptune's largest moon, Tri-
 681 ton, in pink. The ranges in these plasma parameters are obtained from Kivelson et al.
 682 (2004) for the Jovian moons, from Arridge et al. (2011); Khurana et al. (2008); Krupp
 683 et al. (2020); Simon et al. (2009, 2012, 2015) for the Saturnian moons, and from Hansen
 684 et al. (2021) for Triton. We note that Artemyev, Angelopoulos, Halekas, et al. (2017)
 685 have performed a similar comparison between the plasma beta and the *magnetosonic* Mach
 686 number within the magnetotail plasma sheets of Earth and Mars (see their Figure 12).
 687 However, since we compare β to the Alfvénic Mach number, we do not include the vari-
 688 ability of the martian plasma sheet in panel 8b.

689 On the one hand, Figure 8b illustrates that the magnetosheath plasma is rather
 690 unique in comparison to the environments near the outer-planet moons. Besides the most
 691 extreme cases for Callisto or Rhea, and perhaps excluding times when Titan exits Sat-
 692 urn's magnetosphere entirely and is exposed to the Saturnian magnetosheath and solar
 693 wind plasma (e.g., Bertucci et al., 2008, 2015; Feyerabend et al., 2016), the Moon is ex-
 694 posed to a higher beta, higher Alfvénic-Mach-number plasma than any of these other
 695 moons.

696 On the other hand, Figures 8c and 8d illustrate that the lunar plasma environment
 697 is at times similar to the plasma environments of the outer-planet moons. The terres-
 698 trial magnetotail lobe environment (panel 8c) is not too dissimilar from that experienced
 699 by Saturn's inner moons, which are exposed to the low beta, low Mach-number plasma
 700 of the Saturnian magnetosphere. Of these, Tethys, Dione, and Rhea lack dense global
 701 exospheres and their interactions with the Saturnian plasma generate plasma absorp-
 702 tion features—including a cavity in the plasma density and magnetic field compression
 703 signatures—and Alfvén wings that extend from the moons, connecting them with the
 704 polar Saturnian ionosphere (e.g., Khurana et al., 2008; Simon et al., 2015). Further sim-
 705ilarities in the lunar magnetotail lobe plasma can be extended to Triton—whose inter-
 706action with the markedly sub-Alfvénic and highly variable plasma environment may gen-
 707 erate previously undetected Alfvén wing plasma absorption signatures (Liuzzo, Paty, et
 708 al., 2021; Simon et al., 2021), as well as to Io and Europa—which orbit within the strongly
 709 magnetized inner magnetosphere of Jupiter. Indeed, similar plasma interaction features
 710 well-known at these outer-planet moons have also been observed by ARTEMIS during

711 individual encounters with the Moon while located within the magnetotail lobes (e.g.,
 712 Xu et al., 2019; Liuzzo, Poppe, et al., 2021). Near the plasma sheet of the terrestrial mag-
 713 netotail, Figure 8d shows that the high-beta lunar plasma environment resembles the
 714 plasma to which Titan, Ganymede, and Callisto are exposed. While typical values of β
 715 and M_A are highly variable near these objects—especially near Callisto where these plasma
 716 properties span approximately three orders of magnitude—they cover much of the pa-
 717 rameter space that is encountered by the Moon when located near the terrestrial plasma
 718 sheet.

719 However, while the Alfvénic Mach numbers and plasma betas may be similar near
 720 the Moon and these outer-planet satellites, significant differences exist between the ter-
 721 restrial magnetotail and the outer-planet magnetospheres. One such difference arises from
 722 the orientation of the magnetospheric flow compared to the direction of the local mag-
 723 netic field. Near the moons of Jupiter and Saturn, the ambient plasma flow is nearly al-
 724 ways perpendicular to the direction of the magnetospheric background field. Near Nep-
 725 tune’s moon Triton, the local magnetospheric field is never tilted by more than 43° against
 726 the direction of corotation (Liuzzo, Paty, et al., 2021; Cochrane et al., 2022). In com-
 727 parison, the ambient plasma flow near Earth’s Moon when located within a lobe of the
 728 terrestrial magnetotail is almost entirely aligned with the direction of the tail field. While
 729 the plasma flow may be perpendicular to the local field during an individual ARTEMIS
 730 encounter (see, e.g., the case study by Liuzzo, Poppe, et al., 2021), Figure 7 and Table
 731 1 illustrate that on average, the plasma flow component parallel to the field dominates
 732 the perpendicular components (i.e., $V_x \gg V_y, V_z$), at least within the lobes.

733 An additional difference between these environments is driven by internal dynam-
 734 ics of the giant planet magnetospheres. The rapid rotations of Jupiter and Saturn cause
 735 their magnetospheric plasma to continuously bombard the trailing hemispheres of the
 736 outer-planet moons, which are therefore nearly always exposed to an ambient plasma that
 737 drifts past their surfaces at a velocity $|\mathbf{V}| \gg 0$ (reaching up to ~ 300 km/s at Jupiter’s
 738 moon Callisto). In contrast, when located within the plasma sheet for example, the ter-
 739 restrial Moon is rather exposed to a low-velocity plasma that may not preferentially orig-
 740 inate from any direction: as visible in Figure 7 and Table 1, the mean and median val-
 741 ues for all three components of the flow velocity within the sheet are near 0 km/s. Dur-
 742 ing these conditions, the lunar surface is exposed to a warm ambient plasma that sur-
 743 rounds the Moon and lacks any strong, directed flow, unlike the corotating plasma of the

outer-planet magnetospheres. Besides, Io's volcanoes (at Jupiter) Enceladus' plumes (at Saturn) act as a continual source of neutral particles to the magnetospheres of their parent planets, thereby affecting global magnetospheric dynamics; Earth's magnetosphere is not influenced by any analogous processes. Further differences stem from the fact that the largest outer planet moons possess either appreciable ionospheres (in the case of Titan, Triton, and Callisto) or strong internal magnetic fields (in the case of Ganymede) that affect their local electromagnetic environments. Hence, these differences likely contribute to a lunar interaction with the terrestrial plasma that is, at times, vastly different than those exhibited by the outer-planet moons.

In summary, the immense, ten-year-long ARTEMIS data set allows us to constrain the average properties of the terrestrial magnetotail plasma environment near the lunar orbit. Given the range of plasma conditions during a given magnetotail crossing, in addition to the strong variability thereof, the lunar environment may be analogous of the plasma near the outer planet moons, or unique to the magnetotail approximately $60R_E$ downstream of Earth.

759 Data Availability Statement

760 All data used for this study can be obtained from the ARTEMIS homepage ([arTEMIS](http://arTEMIS.ssl.berkeley.edu)
761 [.ssl.berkeley.edu](http://arTEMIS.ssl.berkeley.edu)) or at NASA's CDAWeb (cdaweb.gsfc.nasa.gov).

762 Acknowledgments

763 The authors acknowledge support from NASA/LDAP grant 80NSSC20K0311. The ARTEMIS
764 mission is funded and operated under NASA grant NAS5-02099. We thank J.P. McFadden
765 for use of ESA data, J.E. Bonnell and F. Mozer for use of EFI data, and K.-H. Glassmeier,
766 U. Auster, and W. Baumjohann for the use of FGM data provided under the lead
767 of the Technical University of Braunschweig and with financial support through the German
768 Ministry for Economy and Technology and the German Center for Aviation and
769 Space, Contract 50-OC-0302. The authors are particularly grateful for discussions with
770 V. Angelopoulos, D. Sibeck, S. Simon, and J.Z.D. Mieth that have strengthened the quality
771 of this study. We appreciate input from two anonymous reviewers that have improved
772 the manuscript.

773 **References**

- 774 Angelopoulos, V. (2008, 12). The THEMIS Mission. *Space Science Reviews*, 141(1-
775 4), 5–34. doi: 10.1007/s11214-008-9336-1
- 776 Angelopoulos, V. (2011, 12). The ARTEMIS Mission. *Space Science Reviews*, 165(1-
777 4), 3–25. doi: 10.1007/s11214-010-9687-2
- 778 Arridge, C. S., André, N., Bertucci, C. L., Garnier, P., Jackman, C. M., Németh, Z.,
779 ... Crary, F. J. (2011). Upstream of Saturn and Titan. *Space Science Rev.*,
780 162(1-4), 25–83. doi: 10.1007/s11214-011-9849-x
- 781 Artemyev, A. V., Angelopoulos, V., Halekas, J. S., Runov, A., Zelenyi, L. M., &
782 McFadden, J. P. (2017, 5). Mars’s magnetotail: Nature’s current sheet laboratory. *Journal of Geophysical Research: Space Physics*, 122(5), 5404–5417. doi:
783 10.1002/2017JA024078
- 784 Artemyev, A. V., Angelopoulos, V., Runov, A., & Vasko, I. Y. (2017). Hot Ion
785 Flows in the Distant Magnetotail: ARTEMIS Observations From Lunar Or-
786 bit to \sim 200 RE. *Journal of Geophysical Research: Space Physics*, 122(10),
787 9898–9909. doi: 10.1002/2017JA024433
- 788 Auster, H. U., Glassmeier, K. H., Magnes, W., Aydogar, O., Baumjohann, W.,
789 Constantinescu, D., ... Wiedemann, M. (2008). The THEMIS flux-
790 gate magnetometer. *Space Science Reviews*, 141(1-4), 235–264. doi:
791 10.1007/s11214-008-9365-9
- 792 Bame, S. J., Asbridge, J. R., Felthauser, H. E., Hones, E. W., & Strong, I. B.
793 (1967). Characteristics of the plasma sheet in the Earth’s magnetotail. *Journal
794 of Geophysical Research*, 72(1), 113. doi: 10.1029/jz072i001p00113
- 795 Baumjohann, W. (1993). The near-earth plasma sheet: an ampe/irm perspective
796 wolfgang baumjohann. *Space Science Reviews*, 64(1993), 141–163.
- 797 Behannon, K. (1968). Mapping of the Earth’s bow shock and magnetic tail by Ex-
798 plorer 33. *Journal of Geophysical Research*, 73(3), 907–930. doi: 10.1029/
799 ja073i003p00907
- 800 Behannon, K. (1970). Geometry of the geomagnetic tail. *J Geophys Res*, 75(4), 743–
801 753. doi: 10.1029/ja075i004p00743
- 802 Bertucci, C., Achilleos, N., Dougherty, M. K., Modolo, R., Coates, A. J., Szego,
803 K., ... Young, D. T. (2008, 9). The Magnetic Memory of Titan’s Ionized
804 Atmosphere. *Science*, 321(5895), 1475–1478. doi: 10.1126/science.1159780

- 806 Bertucci, C., Hamilton, D. C., Kurth, W. S., Hospodarsky, G., Mitchell, D., Ser-
807 gis, N., ... Dougherty, M. K. (2015). Titan's interaction with the su-
808 personic solar wind. *Geophysical Research Letters*, 42(2), 193–200. doi:
809 10.1002/2014GL062106
- 810 Bonnell, J. W., Mozer, F. S., Delory, G. T., Hull, A. J., Ergun, R. E., Cully, C. M.,
811 ... Harvey, P. R. (2008). The electric field instrument (EFI) for THEMIS.
812 *Space Science Reviews*, 141(1-4), 303–341. doi: 10.1007/s11214-008-9469-2
- 813 Borovsky, J. E., Thomsen, M. F., Elphic, R. C., Cayton, T. E., & McComas, D. J.
814 (1998, 9). The transport of plasma sheet material from the distant tail to
815 geosynchronous orbit. *Journal of Geophysical Research: Space Physics*,
816 103(A9), 20297–20331. doi: 10.1029/97JA03144
- 817 Bosqued, J. M., Lormant, N., Rème, H., D'Uston, C., Lin, R. P., Anderson, K. A.,
818 ... Wenzel, K.-P. (1996, 5). Moon-solar wind interactions: First results from
819 the WIND/3DP Experiment. *Geophysical Research Letters*, 23(10), 1259–1262.
820 doi: 10.1029/96GL00303
- 821 Cao, X., Halekas, J., Poppe, A., Chu, F., & Glassmeier, K. (2020, 6). The Ac-
822 celeration of Lunar Ions by Magnetic Forces in the Terrestrial Magnetotail
823 Lobes. *Journal of Geophysical Research: Space Physics*, 125(6), 1–12. doi:
824 10.1029/2020JA027829
- 825 Cao, X., Halekas, J. S., Chu, F., Kistler, M., Poppe, A. R., & Glassmeier, K. (2020,
826 10). Plasma Convection in the Terrestrial Magnetotail Lobes Measured Near
827 the Moon's Orbit. *Geophysical Research Letters*, 47(20), 0–3. doi: 10.1029/
828 2020GL090217
- 829 Cochrane, C. J., Persinger, R. R., Vance, S. D., Midkiff, E. L., Castillo-Rogez, J.,
830 Luspay-Kuti, A., ... Prockter, L. M. (2022, 1). Single- and Multi-Pass Mag-
831 netometric Subsurface Ocean Detection and Characterization in Icy Worlds
832 Using Principal Component Analysis (PCA): Application to Triton. *Earth and
833 Space Science*. doi: 10.1029/2021EA002034
- 834 Cowley, S. W. (1981a). Asymmetry effects associated with the x-component of
835 the IMF in a magnetically open magnetosphere. *Planetary and Space Science*,
836 29(8), 809–818. doi: 10.1016/0032-0633(81)90071-4
- 837 Cowley, S. W. (1981b). Magnetospheric asymmetries associated with the y-
838 component of the IMF. *Planetary and Space Science*, 29(1), 79–96. doi:

- 839 10.1016/0032-0633(81)90141-0
- 840 Feyerabend, M., Simon, S., Neubauer, F. M., Motschmann, U., Bertucci, C., Edberg,
841 N. J. T., ... Kurth, W. S. (2016, 1). Hybrid simulation of Titan's interaction
842 with the supersonic solar wind during Cassini's T96 flyby. *Geophysical
843 Research Letters*, 43(1), 35–42. doi: 10.1002/2015GL066848
- 844 Gencturk Akay, I., Kaymaz, Z., & Sibeck, D. G. (2019). Magnetotail boundary
845 crossings at lunar distances: ARTEMIS observations. *Journal of Atmo-
846 spheric and Solar-Terrestrial Physics*, 182(September 2017), 45–60. doi:
847 10.1016/j.jastp.2018.11.002
- 848 Georgescu, E., Plaschke, F., Auster, U., Fornaçon, K. H., & Frey, H. U. (2011).
849 Modelling of spacecraft spin period during eclipse. *Annales Geophysicae*,
850 29(5), 875–882. doi: 10.5194/angeo-29-875-2011
- 851 Goertz, C. K., & Baumjohann, W. (1991). On the thermodynamics of the plasma
852 sheet. *Journal of Geophysical Research*, 96(A12), 20991. Retrieved from
853 <http://doi.wiley.com/10.1029/91JA02128> doi: 10.1029/91JA02128
- 854 Grigorenko, E. E., Kronberg, E. A., Daly, P. W., Ganushkina, N. Y., Lavraud,
855 B., Sauvaud, J., & Zelenyi, L. M. (2016, 10). Origin of low proton-
856 to-electron temperature ratio in the Earth's plasma sheet. *Journal of
857 Geophysical Research: Space Physics*, 121(10), 9985. Retrieved from
858 <https://onlinelibrary.wiley.com/doi/10.1002/2016JA022874> doi:
859 10.1002/2016JA022874
- 860 Halekas, J. S., Brain, D. A., & Holmström, M. (2015, 1). Moon's Plasma Wake. In
861 A. Keiling, C. M. Jackman, & P. A. Delamere (Eds.), *Magnetotails in the solar
862 system* (pp. 149–167). doi: 10.1002/9781118842324.ch9
- 863 Halekas, J. S., Poppe, A. R., Delory, G. T., Sarantos, M., & McFadden, J. P. (2013).
864 Using ARTEMIS pickup ion observations to place constraints on the lunar
865 atmosphere. *Journal of Geophysical Research (Planets)*, 118(1), 81–88. doi:
866 10.1029/2012JE004292
- 867 Hansen, C. J., Castillo-Rogez, J., Grundy, W., Hofgartner, J. D., Martin, E. S.,
868 Mitchell, K., ... Umurhan, O. (2021, 8). Triton: Fascinating Moon, Likely
869 Ocean World, Compelling Destination! *The Planetary Science Journal*, 2(4),
870 137. doi: 10.3847/PSJ/abffd2
- 871 Hardy, D. A., Freeman, J. W., & Hills, H. K. (1976). Plasma Observations in the

- 872 Magnetotail. In *Magnetospheric particles and fields* (pp. 89–98). doi: 10.1007/
873 978-94-010-1503-5__9
- 874 Hardy, D. A., Hills, H. K., & Freeman, J. W. (1979). Occurrence of the Lobe Plasma
875 At Lunar Distance. *Journal of Geophysical Research: Space Physics*, 84(A1),
876 72–78. doi: 10.1029/ja084ia01p00072
- 877 Holmström, M., Fatemi, S., Futaana, Y., & Nilsson, H. (2012, 2). The interaction
878 between the Moon and the solar wind. *Earth, Planets and Space*, 64(2), 237–
879 245. doi: 10.5047/eps.2011.06.040
- 880 Kaymaz, Z., Siscoe, G. L., Luhmann, J. G., Lepping, R. P., & Russell, C. T. (1994).
881 Interplanetary magnetic field control of magnetotail magnetic field geometry:
882 IMP 8 observations. *Journal of Geophysical Research*, 99(A6), 11113. doi:
883 10.1029/94ja00300
- 884 Khurana, K. K., Russell, C. T., & Dougherty, M. K. (2008, 2). Magnetic portraits of
885 Tethys and Rhea. *Icarus*, 193(2), 465–474. doi: 10.1016/j.icarus.2007.08.005
- 886 Kiehas, S. A., Runov, A., Angelopoulos, V., Hietala, H., & Korovinksiy, D. (2018).
887 Magnetotail Fast Flow Occurrence Rate and Dawn-Dusk Asymmetry at
888 XGSM ~60 RE. *Journal of Geophysical Research: Space Physics*, 123(3),
889 1767–1778. doi: 10.1002/2017JA024776
- 890 Kivelson, M., Bagenal, F., Kurth, W., Neubauer, F., Paranicas, C., & Saur, J.
891 (2004). Magnetospheric interactions with satellites. *Jupiter: The planet,
892 satellites and magnetosphere*, m, 513–536.
- 893 Krupp, N., Kotova, A., Roussos, E., Simon, S., Liuzzo, L., Paranicas, C., ... Jones,
894 G. H. (2020, 6). Magnetospheric Interactions of Saturn's Moon Dione
895 (2005–2015). *Journal of Geophysical Research: Space Physics*, 125(6). doi:
896 10.1029/2019JA027688
- 897 Lavraud, B., Borovsky, J. E., Génot, V., Schwartz, S. J., Birn, J., Fazakerley, A. N.,
898 ... Wild, J. A. (2009, 9). Tracing solar wind plasma entry into the magnetosphere
899 using ion-to-electron temperature ratio. *Geophysical Research Letters*,
900 36(18), L18109. doi: 10.1029/2009GL039442
- 901 Liuzzo, L., Paty, C., Cochrane, C., Nordheim, T., Luspay-Kuti, A., Castillo-Rogez,
902 J., ... Prockter, L. (2021). Triton's Variable Interaction With Neptune's Mag-
903 netospheric Plasma. *Journal of Geophysical Research: Space Physics*, 126(11),
904 1–27. doi: 10.1029/2021ja029740

- 905 Liuzzo, L., Poppe, A. R., Halekas, J. S., Simon, S., & Cao, X. (2021, 5). Investigating the Moon's Interaction With the Terrestrial Magnetotail Lobe Plasma.
906
907 *Geophysical Research Letters*, 48(9), 1–11. doi: 10.1029/2021GL093566
- 908 Matsumoto, Y., Mukai, T., Saito, Y., Kokubun, S., & Hoshino, M. (2001, 11).
909 On the pressure balance in the distant magnetotail. *Journal of Geophysical*
910 *Research: Space Physics*, 106(A11), 25905–25917. Retrieved from <http://doi.wiley.com/10.1029/2001JA900064> doi: 10.1029/2001JA900064
- 911
912 McFadden, J., Carlson, C., Larson, D., Bonnell, J., Mozer, F., Angelopoulos, V., ...
913 Auster, U. (2008). THEMIS ESA first science results and performance issues.
914 *Space Science Reviews*, 141(1-4), 477–508. doi: 10.1007/s11214-008-9433-1
- 915 McFadden, J., Carlson, C., Larson, D., Ludlam, M., Abiad, R., Elliott, B., ...
916 Angelopoulos, V. (2008). The THEMIS ESA plasma instrument and
917 in-flight calibration. *Space Science Reviews*, 141(1-4), 277–302. doi:
918 10.1007/s11214-008-9440-2
- 919 Meng, C.-I., & Anderson, K. A. (1974, 12). Magnetic field configuration in the mag-
920 netotail near 60 R E. *Journal of Geophysical Research*, 79(34), 5143–5153. doi:
921 10.1029/JA079i034p05143
- 922 Michel, F. C. (1968, 12). Lunar wake at large distances. *Journal of Geophysical Re-*
923 *search*, 73(23), 7277–7283. doi: 10.1029/JA073i023p07277
- 924 Mieth, J. Z. D., Fröhlauff, D., & Glassmeier, K.-H. (2019, 3). Statistical analysis of
925 magnetopause crossings at lunar distances. *Annales Geophysicae*, 37(2), 163–
926 169. doi: 10.5194/angeo-37-163-2019
- 927 Mihalov, J. D., Colburn, D. S., Currie, R. G., & Sonett, C. P. (1968, 2). Con-
928 figuration and reconnection of the geomagnetic tail. *Journal of Geophysical*
929 *Research*, 73(3), 943–959. Retrieved from <http://doi.wiley.com/10.1029/JA073i003p00943> doi: 10.1029/JA073i003p00943
- 930
931 Mittelholz, A., Grayver, A., Khan, A., & Kuvshinov, A. (2021). The Global Con-
932 ductivity Structure of the Lunar Upper and Mid Mantle. *Journal of Geophysi-*
933 *cal Research: Planets*, 1–22. doi: 10.1029/2021je006980
- 934 Ness, N. F. (1965, 2). The magnetohydrodynamic wake of the Moon. *Journal of*
935 *Geophysical Research*, 70(3), 517–534. doi: 10.1029/JZ070i003p00517
- 936 Ness, N. F. (1972). Interaction of the Solar Wind with the Moon. In (pp. 347–
937 393). Retrieved from <http://link.springer.com/10.1007/978-94-009-3693>

- 938 -5_21 doi: 10.1007/978-94-009-3693-5_{\}}21
- 939 Nguyen, G., Aunai, N., Welle, B. d., Jeandet, A., Lavraud, B., & Fontaine, D. (2021,
940 12). Massive multi-mission statistical study and analytical modeling of the
941 Earth's magnetopause: 2 – Shape and location. *Journal of Geophysical Re-*
942 *search: Space Physics*, 1–21. doi: 10.1029/2021JA029774
- 943 Poppe, A. R. (2019, 8). Comment on “The Dominant Role of Energetic Ions
944 in Solar Wind Interaction With the Moon” by Omidi et al. *Journal of*
945 *Geophysical Research: Space Physics*, 124(8), 6927–6932. Retrieved from
946 <https://onlinelibrary.wiley.com/doi/10.1029/2019JA026692> doi:
947 10.1029/2019JA026692
- 948 Poppe, A. R., Samad, R., Halekas, J. S., Sarantos, M., Delory, G. T., Farrell, W. M.,
949 ... McFadden, J. P. (2012). ARTEMIS observations of lunar pick-up ions in
950 the terrestrial magnetotail lobes. *Geophysical Research Letters*, 39(17), 1–6.
951 doi: 10.1029/2012GL052909
- 952 Runov, A., Angelopoulos, V., Artemyev, A., Lu, S., & Zhou, X. Z. (2018). Near-
953 Earth Reconnection Ejecta at Lunar Distances. *Journal of Geophysical Re-*
954 *search: Space Physics*, 123(4), 2736–2744. doi: 10.1002/2017JA025079
- 955 Sarris, E. T., Krimigis, S. M., Lui, A. T. Y., Ackerson, K. L., Frank, L. A., &
956 Williams, D. J. (1981, 4). Relationship between energetic particles and plas-
957 mas in the distant plasma sheet. *Geophysical Research Letters*, 8(4), 349–352.
958 doi: 10.1029/GL008i004p00349
- 959 Sibeck, D. G., & Murphy, K. R. (2021, 4). Large-Scale Structure and Dynamics of
960 the Magnetosphere. In (Vol. 2, pp. 15–36). doi: 10.1002/9781119815624.ch2
- 961 Sibeck, D. G., Siscoe, G. L., Slavin, J. A., & Lepping, R. P. (1986). Major flatten-
962 ing of the distant geomagnetic tail. *Journal of Geophysical Research*, 91(A4),
963 4223. doi: 10.1029/JA091iA04p04223
- 964 Sibeck, D. G., Siscoe, G. L., Slavin, J. A., Smith, E. J., Tsurutani, B. T., & Lep-
965 ping, R. P. (1985). The distant magnetotail's response to a strong interplane-
966 tary magnetic field B_y : Twisting, flattening, and field line bending. *Journal*
967 *of Geophysical Research*, 90(A5), 4011. doi: 10.1029/JA090iA05p04011
- 968 Simon, S., Addison, P., & Liuzzo, L. (2021, 12). Formation of a Displaced Plasma
969 Wake at Neptune's Moon Triton. *Journal of Geophysical Research: Space*
970 *Physics*, 127(e2021JA029958). doi: 10.1029/2021JA029958

- 971 Simon, S., Kriegel, H., Saur, J., Wennmacher, A., Neubauer, F. M., Roussos, E.,
972 ... Dougherty, M. K. (2012, 7). Analysis of Cassini magnetic field observa-
973 tions over the poles of Rhea. *Journal of Geophysical Research: Space Physics*,
974 117(A7), n/a-n/a. doi: 10.1029/2012JA017747
- 975 Simon, S., Roussos, E., & Paty, C. (2015). The interaction between Saturn's moons
976 and their plasma environments. *Physics Reports*, 602, 1–65.
- 977 Simon, S., Saur, J., Neubauer, F. M., Motschmann, U., & Dougherty, M. K. (2009).
978 Plasma wake of Tethys: hybrid simulations versus Cassini MAG data. *Geo-
979 phys. Res. Lett.*, 36(4), L04108. doi: 10.1029/2008GL036943
- 980 Slavin, J. A., Smith, E. J., Sibeck, D. G., Baker, D. N., Zwickl, R. D., & Akasofu,
981 S.-I. (1985). An ISEE 3 study of average and substorm conditions in the
982 distant magnetotail. *Journal of Geophysical Research*, 90(A11), 10875. doi:
983 10.1029/ja090ia11p10875
- 984 Vasko, I. Y., Petrukovich, A. A., Artemyev, A. V., Nakamura, R., & Zelenyi, L. M.
985 (2015, 10). Earth's distant magnetotail current sheet near and beyond lunar
986 orbit. *Journal of Geophysical Research: Space Physics*, 120(10), 8663–8680.
987 doi: 10.1002/2015JA021633
- 988 Wang, C.-P., Gkioulidou, M., Lyons, L. R., & Angelopoulos, V. (2012, 8). Spatial
989 distributions of the ion to electron temperature ratio in the magnetosheath
990 and plasma sheet. *Journal of Geophysical Research: Space Physics*, 117(A8),
991 n/a-n/a. doi: 10.1029/2012JA017658
- 992 Wang, C.-P., Liu, Y. H., Xing, X., Runov, A., Artemyev, A., & Zhang, X. (2020).
993 An Event Study of Simultaneous Earthward and Tailward Reconnection Ex-
994 haust Flows in the Earth's Midtail. *Journal of Geophysical Research: Space
995 Physics*, 125(6), 1–20. doi: 10.1029/2019JA027406
- 996 Wang, C.-P., Lyons, L. R., & Angelopoulos, V. (2014, 9). Properties of low-latitude
997 mantle plasma in the Earth's magnetotail: ARTEMIS observations and global
998 MHD predictions. *Journal of Geophysical Research: Space Physics*, 119(9),
999 7264–7280. doi: 10.1002/2014JA020060
- 1000 Wing, S., Johnson, J. R., Chaston, C. C., Echim, M., Escoubet, C. P., Lavraud, B.,
1001 ... Wang, C.-P. (2014, 11). Review of Solar Wind Entry into and Trans-
1002 port Within the Plasma Sheet. *Space Science Reviews*, 184(1-4), 33–86. doi:
1003 10.1007/s11214-014-0108-9

- 1004 Xu, X., Xu, Q., Chang, Q., Xu, J., Wang, J., Wang, Y., ... Angelopoulos, V.
1005 (2019). ARTEMIS Observations of Well-structured Lunar Wake in Subsonic
1006 Plasma Flow. *The Astrophysical Journal*, 881(1), 76. doi: 10.3847/1538-4357/
1007 ab2e0a
- 1008 Yamamoto, T., Shiokawa, K., & Kokubun, S. (1994, 12). Magnetic field structures
1009 of the magnetotail as observed by GEOTAIL. *Geophysical Research Letters*,
1010 21(25), 2875–2878. doi: 10.1029/94GL01609
- 1011 Zhang, H., Khurana, K. K., Kivelson, M. G., Angelopoulos, V., Wan, W. X., Liu,
1012 L. B., ... Liu, W. L. (2014). Three-dimensional lunar wake reconstructed
1013 from ARTEMIS data. *Journal of Geophysical Research: Space Physics*, 119(7),
1014 5220–5243. doi: 10.1002/2014JA020111
- 1015 Zhou, X.-Z., Angelopoulos, V., Poppe, A. R., & Halekas, J. S. (2013). ARTEMIS
1016 observations of lunar pickup ions: Mass constraints on ion species. *Journal of*
1017 *Geophysical Research (Planets)*, 118(9), 1766–1774. doi: 10.1002/jgre.20125
- 1018 Zwickl, R. D., Baker, D. N., Bame, S. J., Feldman, W. C., Gosling, J. T., Hones,
1019 E. W., ... Slavin, J. A. (1984). Evolution of the Earth's distant magnetotail:
1020 ISEE 3 electron plasma results. *Journal of Geophysical Research*, 89(A12),
1021 11007. doi: 10.1029/JA089iA12p11007